J. Fluid Mech. (2017), *vol.* 818, *pp.* 528–561. © Cambridge University Press 2017
doi:10.1017/jfm.2017.120

Mechanism of frequency lock-in in transonic buffeting flow

Chuanqiang Gao[1], Weiwei Zhang[1,†], Xintao Li[1], Yilang Liu[1], Jingge Quan[1], Zhengyin Ye[1] and Yuewen Jiang[2]

[1]School of Aeronautics, Northwestern Polytechnical University, Xi'an 710072, China

[2]Department of Engineering Science, University of Oxford, Oxford OX2 0ES, UK

(Received 8 July 2016; revised 13 February 2017; accepted 19 February 2017;
first published online 5 April 2017)

Frequency lock-in can occur on a spring suspended airfoil in transonic buffeting flow, in which the coupling frequency does not follow the buffet frequency but locks onto the natural frequency of the elastic airfoil. Most researchers have attributed this abnormal phenomenon to resonance. However, this interpretation failed to reveal the root cause. In this paper, the physical mechanism of frequency lock-in is studied by a linear dynamic model, combined with the coupled computational fluid dynamics/computational structural dynamics (CFD/CSD) simulation. We build a reduced-order model of the flow using the identification method and unsteady Reynolds-averaged Navier–Stokes computations in a post-buffet state. A linear aeroelastic model is then obtained by coupling this model with a degree-of-freedom equation for the pitching motion. Results from the complex eigenvalue analysis indicate that the coupling between the structural mode and the fluid mode leads to the instability of the structural mode. The instability range coincides with the lock-in region obtained by the coupled CFD/CSD simulation. Therefore, the physical mechanism underlying frequency lock-in is caused by the linear coupled-mode flutter – the coupling between one structural mode and one fluid mode. This is different from the classical single-degree-of-freedom flutter (e.g. transonic buzz), which occurs in stable flows; the present flutter is in the unstable buffet flow. The response of the airfoil system undergoes a conversion from forced vibration to self-sustained flutter. The coupling frequency certainly should lock onto the natural frequency of the elastic airfoil.

Key words: flow–structure interactions, low-dimensional models, shock waves

1. Introduction

Transonic buffet is an aerodynamic phenomenon of self-sustained shock oscillations and dramatic lift fluctuations that occur with a certain combination of Mach number and mean angle of attack, the onset of which is linked to a global instability (Crouch *et al.* 2009; Sartor *et al.* 2015*b*; Kou & Zhang 2017). These shock oscillations are regarded as a result of shock–boundary layer interaction (Lee 2001). Transonic buffet,

† Email address for correspondence: aeroelastic@nwpu.edu.cn

especially the consequent unsteady load, has a negative influence on the fatigue life of the aircraft. Therefore, the investigation on transonic buffet has important theoretical and practical values in aeronautical engineering.

In the classical conception of aeroelasticity, transonic buffeting is considered to be a dynamic response problem and is believed to be a type of forced vibration under the unstable buffet flow, in the process of which the interaction between the fluid and the solid is ignored. Based on this viewpoint, most investigations, wind tunnel experiments (McDevitt & Okuno 1985; Jacquin *et al.* 2009; Doerffer, Hirsch & Dussauge 2010; Hartmann, Feldhusen & Schröder 2013*a*) and numerical simulations (Deck 2005; Xiao, Tsai & Liu 2006; Chen, Xu & Lu 2010; Sengupta *et al.* 2013; Grossi, Braza & Hoarau 2014; Iovnovich & Raveh 2015) were performed on rigid stationary wings/airfoils. These wind tunnel experiments provided detailed experimental status and abundant data, which have been used as standard examples to validate the computational fluid dynamics (CFD) codes. The numerical simulations focus on the prediction of buffet onsets, periodic buffet flows and unsteady buffet loads based on CFD tools with different levels of precision.

Recently, Raveh & Dowell (2014) studied the aeroelastic responses of an elastically mounted airfoil system in transonic buffeting flow by numerical simulations. In classical aeroelasticity, the airfoil would display a forced vibration due to the unstable buffet flow. Thus, the airfoil oscillation frequency should depend on the buffet frequency. However, it is found that it no longer follows the buffet frequency but locks onto the natural frequency of the elastic system when the natural frequency approaches the buffet frequency. Simultaneously, a larger oscillating amplitude of the airfoil is observed within the lock-in region, which is dangerous to the aircraft. This abnormal phenomenon is often referred to as 'frequency lock-in' in transonic buffeting flow. It is firstly investigated on a NACA0012 airfoil undergoing a prescribed harmonic oscillation in transonic buffeting flows (Raveh & Dowell 2011). And in a wind tunnel experiment, Hartmann, Klaas & Schröder (2013*b*) also observed the phenomenon of frequency lock-in.

The above phenomenon is very similar to the frequency lock-in founded in vortex-induced vibration (VIV) of flow past a cylinder (Blevins 1990). They are both an oscillation of the spring suspend airfoil/cylinder with an increasing amplitude in a periodic unstable flow, and the oscillation frequency follows the natural frequency of the elastic system rather than the frequency of the unstable flow. The frequency lock-in phenomenon in VIV has been extensively studied based on either experimental or numerical methods, such as the effects of Reynolds number (Govardhan & Williamson 2006), mass ratio (Prasanth, Premchandran & Mittal 2011) and structural damping coefficient (Nguyen *et al.* 2012) in the lock-in region. Most researchers attributed its inducement in VIV to resonance (Govardhan & Williamson 2002; Willden & Graham 2006). The large-amplitude oscillation occurs when the cylinder natural frequency is comparable with the vortex shedding frequency, which corresponds to the conventional resonance theory. The frequency lock-in in transonic buffeting flow is also attributed to the nonlinear aerodynamic resonance (Raveh & Dowell 2011, 2014; Hartmann *et al.* 2013*a*), inheriting the classic concept from VIV. The resonance process is as follows. As the frequency of the buffet flow approaches that of the elastic airfoil system, the oscillating aerodynamic forces cause an increasing amplitude of motion, which corresponds to a standard resonance effect. Then, if this amplitude is large enough, the buffeting flow is somehow affected and forced to move at the natural resonating frequency of the elastic airfoil system. This feedback process is implicitly assumed to be nonlinear, as the existence of lock-in and its

region depend on the oscillation amplitude. However, the interpretation that frequency lock-in is caused by simple resonance has its limitations. For example, Singh & Mittal (2005) conducted numerical simulations to investigate VIV and found that the maximum vibration amplitude of the cylinder was acquired at the ratio of the natural frequency of the elastic system to the unstable flow frequency $k_s/k_b \sim 1.28$ rather than at the synchronized point $k_s/k_b \sim 1.0$. Quan *et al.* (2016) studied the characteristics of frequency lock-in in transonic buffeting flow by the coupled computational fluid dynamics/computational structural dynamics (CFD/CSD) simulation method. Results showed that the maximum vibration amplitude of the NACA 0012 airfoil was obtained at the frequency ratio $k_s/k_b \sim 1.5$, and the lock-in phenomenon still existed when it was enlarged to $k_s/k_b \sim 2.4$. Besides, the lock-in region did not display a symmetrical distribution against the buffet frequency as expected by resonance theory (Singh & Mittal 2005; Raveh & Dowell 2011; Besem *et al.* 2016), but it is often located on the side of higher frequency, which was obvious in the coupled CFD/CSD simulations (Singh & Mittal 2005; Quan *et al.* 2016). These anomalies are difficult to explain from the perspective of resonance.

In the study of VIV in cylinder wake flow, different interpretations have been proposed based on the linear analytical model. De Langre (2006) utilized a semi-empirical and linearized wake oscillator model, in which all nonlinear and dissipative terms were neglected. The resulting linear system was constructed by coupling the wake oscillator model and the structural oscillator. Stability analysis results showed that frequency lock-in was primarily caused by the coupled-mode flutter instead of the nonlinear resonance. This analytical idea opened a new threshold for the interpretation of the frequency lock-in phenomenon in VIV. Quite recently, Zhang *et al.* (2015*c*) constructed a linear reduced-order model (ROM) based on the system identification method to study VIV at low Reynolds numbers. Results from the ROM showed that the frequency lock-in phenomenon could be divided into two patterns, resonance-induced lock-in and flutter-induced lock-in, according to different inducing mechanisms. It provides a comprehensive understanding of mechanisms of the frequency lock-in in VIV.

What are the physical mechanism of the frequency lock-in phenomenon and the consequence of the oscillation with a large amplitude in transonic buffeting flow? The key to answering this question is to construct an appropriate fluid model for the post-buffet flow, since it is simple to construct a structural model. Different from the cylinder wake flow, for which many semi-analytical or semi-empirical models have been proposed, there are no such models in transonic buffet flow. The current widely used CFD method is a nonlinear and high-order model, which can help display details of flow structures, but it is not convenient to analyse the mechanism. Therefore, the premise in the study of the lock-in mechanism is to set up a low-order but high accuracy linear ROM, which has an advantage of distinctly displaying the physical mechanism associated with stability. In this paper, we construct a CFD-based ROM for the unsteady aerodynamics of a pitching NACA 0012 airfoil in transonic buffeting flow by using a system identification method. By coupling the CFD-based ROM with the structural motion equation the ROM-based model is constructed. Eigenvalue analysis of this aeroelastic model is then performed to study the mechanism underlying the frequency lock-in phenomenon in transonic buffeting flow at $M = 0.7$, $Re = 3 \times 10^6$ and $\alpha = 5.5°$. A coupled CFD/CSD simulation is simultaneously conducted to validate results analysed by the ROM-based aeroelastic model.

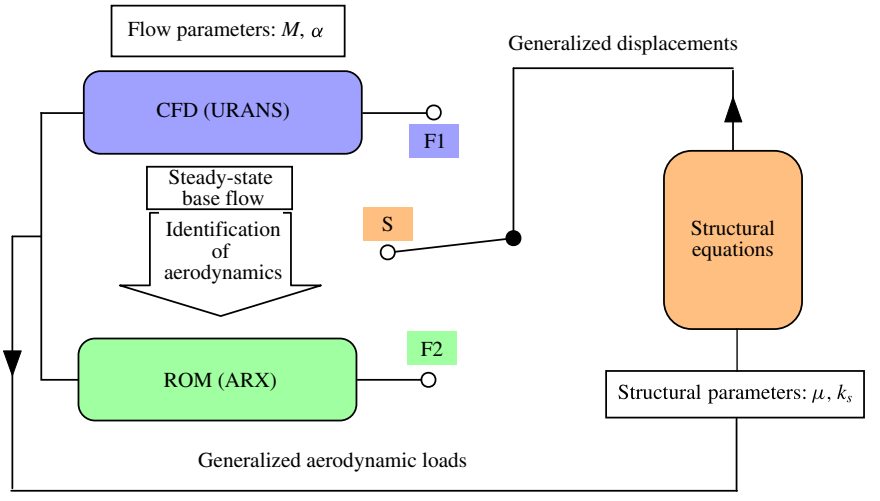

FIGURE 1. (Colour online) Block diagram of the models and their relationship.

2. A brief introduction to the models

This section will briefly introduce the methods/models used in the next three sections and their relationship. As shown in figure 1, for the transonic buffet flow, there are two ways/models to obtain the unsteady generalized aerodynamic loads. One is CFD simulation with the unsteady Reynolds-averaged Navier–Stokes (URANS) method (the blue block), of which details and validation will be presented in § 3. The other is the ROM (the green block) with an external input by the system identification method. The building of the ROM is based on the CFD data; therefore, it has a considerable accuracy and higher efficiency compared with CFD. In § 4, the process and the validation of the ROM will be discussed. We then establish the aeroelastic model by coupling the fluid model with the structural equations. There are also two strategies, which are decided by the way to obtain the unsteady generalized aerodynamic loads. As shown in figure 1, when the block of the structural equations (S) connects with the CFD (F1), we obtain the coupled CFD/CSD simulation method. However, when the structural block connects with the ROM (F2), it is the ROM-based aeroelastic model. These will be discussed in § 5.

3. Numerical method and its validation

Periodic shock motions in transonic buffet occur on time scales that are much longer than those of wall-bounded turbulence, so a numerical simulation performed solving the URANS equations is justified (Crouch *et al.* 2009; Sartor, Mettot & Sipp 2015*a*; Sartor *et al.* 2015*b*). Many numerical simulations based on the URANS method have been performed since the 1990s. In particular, numerical scheme, turbulence model, time step size and grid influences have been studied. Barakos & Drikakis (2000) assessed the adequacy of several turbulence models, including the Baldwin–Lomax model, Spalart–Allmaras (S–A) model, linear and nonlinear k–ε models and a nonlinear k–ω model, for transonic buffet simulations. The S–A turbulence model predicted the transonic buffet onset at slightly higher angles of attack than those in the wind tunnel test. Some researchers, such as Goncalves & Houdeville (2004), Xiao *et al.* (2006), Crouch *et al.* (2009), Raveh & Dowell (2011, 2014) and Sartor *et al.* (2015*a*), computed transonic buffet using the URANS method and the S–A turbulence model.

3.1. *Flow governing equations*

In this study, the flow analysis of the NACA0012 airfoil is performed by an in-house hybrid-unstructured flow solver which solves the URANS equations by a cell-centred finite volume approach. The integral form of the two-dimensional compressible URANS equations with the S–A turbulence model can be written for a cell of volume V limited by a surface S. The equation can be expressed as:

$$\frac{\partial}{\partial t}\int_V \boldsymbol{W}\,\mathrm{d}V + \oint_S \boldsymbol{E}^i(\boldsymbol{W}, \boldsymbol{V}_{grid})\cdot\boldsymbol{n}\,\mathrm{d}S - \oint_S \boldsymbol{E}^v(\boldsymbol{W})\cdot\boldsymbol{n}\,\mathrm{d}S = \int_V \boldsymbol{H}\,\mathrm{d}V, \tag{3.1}$$

where $\boldsymbol{n}$ represents the outer unit normal vector to the boundary S; $\boldsymbol{W}$ is a five-component vector of conservative variables, $\boldsymbol{W} = [\rho \;\; \rho u \;\; \rho v \;\; \rho E \;\; \rho\tilde{\nu}]^{\mathrm{T}}$. ρ is the density; u, v are the x and y components of the velocity vector of the flow; E denotes the specific total energy; and $\tilde{\nu}$ denotes the working variable of the S–A turbulence model. $\boldsymbol{E}^i(\boldsymbol{W}, \boldsymbol{V}_{grid})$ and $\boldsymbol{E}^v(\boldsymbol{W})$ are the inviscid flux and the viscous flux, respectively. $\boldsymbol{H}$ is the source term.

The spatial discretization and time integration of the turbulence model equation and mean flow equations are carried out in a loosely coupled way. The second-order advection upstream splitting method (AUSM) + scheme is conducted to evaluate the inviscid flux, with a reconstruction technique based on the least-squares approach. High-order reconstruction schemes refer to Liu *et al.* (2016). The grid velocity $\boldsymbol{V}_{grid}$ is modified according to the geometric conservation law (Hyung & Yannis 2006) when CFD/CSD simulations are performed. The viscous flux term is discretized by the standard central scheme. In the turbulence model, the transport equation for the working variable $\hat{\upsilon}$ is given by the standard form proposed by Spalart & Allmaras (1992). Many reports have indicated that the S–A turbulence model with a second-order scheme is accurate enough to predict the flow instability (Crouch, Garbaruk & Magidov 2007; Sartor *et al.* 2015*a*; Sartor & Timme 2017). The convective and source terms are discretized by the second-order AUSM + scheme, and the destruction and diffusion terms by the second-order central scheme in the present study. For unsteady computations, the dual time stepping method, proposed by Jameson (1991), is used to solve the governing equations. At the sub-iteration, the fourth stage Runge–Kutta scheme is used with local time stepping and residual smoothing to accelerate the convergence. Details of the numerical method can be found in Zhang *et al.* (2015*b*) and Gao, Zhang & Ye (2016*a*).

A no-slip wall boundary condition is applied to the airfoil surface. The location and velocity of the airfoil are updated at each real time step due to the pitching motion of the airfoil. Moreover, the far field boundary is assigned a non-reflective boundary condition based on Riemann invariants to ensure that the disturbance generated by the object does not return to the flow field.

A moving boundary is involved in the simulation due to the airfoil pitching motion when the frequency lock-in is simulated. Thus, a grid deformation method must be used to match the grid with the new wall boundary condition. The scheme of the computational grid deformation is based on radial basis function (RBF) interpolation (De Boer, Van der Schoot & Bijl 2007; Wang, Mian & Ye 2015). A compact Wendland's C2 function (De Boer *et al.* 2007) is chosen as the basis function.

3.2. *Validation of the CFD method*

Validation of CFD results is performed based on a transonic buffet wind tunnel test by Doerffer *et al.* (2010). They performed a wind tunnel test on a NACA0012 airfoil at

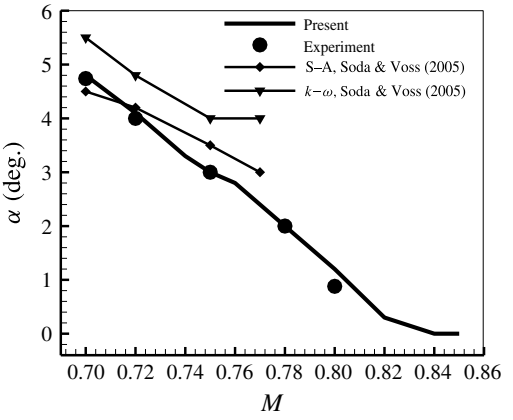

FIGURE 2. Buffet onset boundaries calculated with different CFD codes at Mach numbers from 0.7 to 0.8, and $Re = 3 \times 10^6$.

Mach numbers from 0.7 to 0.8, at a Reynolds number of 3×10^6 and within a range of angles of attack including the buffet onset. In this experimental test, the buffet frequency at $M = 0.7$ and $\alpha = 5^\circ$ is 74 Hz, which is 0.176 in the non-dimensional reduced frequency scale. The reduced buffet frequency is defined as $k_b = \pi f_b c/U_\infty$. f_b is the buffet frequency; c indicates the chord of the airfoil; and U_∞ denotes the velocity of the free stream.

The computational hybrid-unstructured flow solver has 25, 361 nodes and 40 layers of structured viscous grid around the airfoil. The distance between the first layer and the wall in the perpendicular direction is 5×10^{-6} chords ($y^+ \sim 1$). The time step for the CFD simulation is 2.94×10^{-4} s. Figure 2 shows the comparison of the transonic buffet onset boundary for the NACA0012 airfoil. The circles are from the experiment of Doerffer *et al.* (2010) and the clean solid line is from the URANS method. It also shows the results from Soda & Voss (2005), in which the boundaries are larger than those of the experimental data. The experiment and URANS calculations are in very good agreement. At $M = 0.7$, the calculated buffet onset angle is 4.80°, which is very close to the 4.74° tested by Doerffer *et al.* (2010). Time histories of the lift coefficient at 4.6°, 4.8° and 5.5° are shown in figure 3. It can be seen that the dramatic unsteady loads occur at 5.5°. Therefore, further investigation of the lock-in phenomenon is performed at $M = 0.7$ and $\alpha = 5.5^\circ$. Figure 4 shows reduced buffet frequencies at different angles of attack at $M = 0.7$. As the angle of attack increases, the buffet frequency increases smoothly and slightly. At $\alpha = 5^\circ$, the reduced frequency is 0.180, which is very close to the experimental data. For the scale of Strouhal number, $St = f_b c/U_\infty$, it is approximately 0.058. McDevitt & Okuno (1985) obtained $St = 0.045$–0.070 on the NACA0012 airfoil. These results indicate that the numerical method in this paper is accurate for the simulation of transonic buffet. The convergence of the grid and the time step are presented in appendix B. For more validation of the URANS method, one can refer to our earlier studies (Gao *et al.* 2015; Zhang *et al.* 2015*b*).

The grid deformation method is important to the coupled CFD/CSD simulation. The validation of this method and the numerical algorithm are tested on a forced harmonic pitching NACA 0012 airfoil from the CT5 case by Landon (1982). Details of the case and validated results are both presented in our research in Gao *et al.* (2015) and

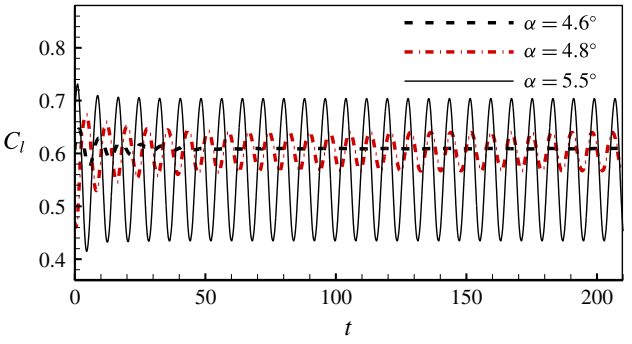

FIGURE 3. (Colour online) The lift and moment responses at $\alpha = 4.6°$, $\alpha = 4.8°$ and $\alpha = 5.5°$ at $M = 0.7$ and $Re = 3 \times 10^6$.

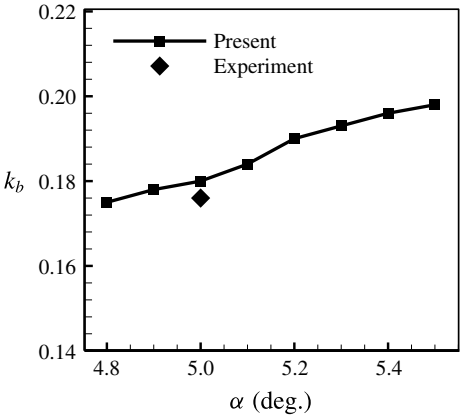

FIGURE 4. Buffet frequencies at different angles of attack, $M = 0.7$ and $Re = 3 \times 10^6$.

Zhang *et al.* (2015*b*). The method is appropriate for the present investigation on the frequency lock-in.

4. Modelling of unsteady aerodynamics

4.1. *Reduced-order modelling by system identification*

The application of the ROM to unsteady aerodynamics has been an active area of research in recent years (Lucia, Beran & Silva 2004; Ghoreyshi, Jirasek & Cummings 2014). It is desirable to use a relatively simple but accurate approximation for unsteady aerodynamics by a ROM with a small number of orders (typically less than one hundred) rather than the full-order CFD model. Popular ROMs are mainly based on proper orthogonal decomposition (POD) and the system identification method. They have been successfully performed to study thrust modelling for a flapping airfoil (Li *et al.* 2017), flutter in transonic flow (Hall, Thomas & Dowell 2000; Thomas *et al.* 2006; Zhang, Chen & Ye 2015*a*), aeroservoelasticity (Zhang & Ye 2007; Zhang, Ye & Zhang 2009; Huang *et al.* 2015) and unstable flow control (Barbagallo, Sipp & Schmid 2009; Juillet, Schmid & Huerre 2013). To solve the above-mentioned stability problems, one needs to establish a dynamic linear model

under a slight structural disturbance even if the flow contains some nonlinear features, such as the shock wave and separation. However, for the limit-cycle oscillation (LCO) in transonic flow, if larger shock motions are involved, the nonlinearity becomes the dominant characteristic. Zhang, Wang & Ye (2012) established a nonlinear unsteady aerodynamic ROM using the RBF neural network, and accurately predicted LCOs with large shock motions in transonic flow. It became a hot topic to model nonlinear and unsteady aerodynamics (He, Yang & Gu 2014; Mannarino & Mantegazza 2014; Huang *et al.* 2015). Very recently, Gao, Zhang & Ye (2016*b*) studied the transonic buzz based on the ROM in pre-buffet flow. However, these ROMs were conducted by the forced perturbation based on stable flows. To the authors' knowledge, they have not been documented in unstable transonic buffet flows.

We are interested in constructing a linear model to analyse the underlying mechanism of the lock-in phenomenon rather than a nonlinear model just to reproduce complex responses. This linear model is constructed based on the system identification method. The transonic buffet flow discussed in the present study is unstable, and this makes it a challenging construction for two reasons:

(i) The linear ROM must be set up based on the unstable steady-state base flow. However, it is a challenge to obtain the unstable steady solution of the transonic buffet flow.

(ii) In the training process, a competition exists between the unstable buffet flow itself and the unsteadiness caused by the forced pitching airfoil. Therefore, the other challenge is to design an appropriate forcing signal to avoid the training behaving nonlinearly.

The ROM on the basis of ARX (Auto Regressive with eXogenous input) is introduced in detail in our previous study (Zhang & Ye 2007), and it has been successfully performed in the investigation of VIV at supercritical Reynolds numbers (Zhang *et al.* 2015*c*). For the unstable flow, the modelling process contains three steps – obtaining the unstable steady base flow, training and then performing identification. In this paper, the modelling of the transonic buffet flow is also based on the ARX model. Given that the unsteady loads are computed in a discrete domain, the single-input–single-output model can be expressed as follows:

$$y_a(k) = \sum_{i=1}^{na} A_i y_a(k-i) + \sum_{i=0}^{nb-1} B_i u(k-i), \tag{4.1}$$

where y_a is the system output (pitching moment coefficient C_m) and u is the system input (pitching angle θ). A_i and B_i are constant coefficients to be estimated. Orders of the model chosen by the user are na and nb. The least-squares method is used to estimate unknown model parameters. To guarantee the mean data are zero, the constant levels need to be removed from the initial data before they are estimated.

In order to complete the state-space aeroelastic analysis, we define a state vector $\boldsymbol{x_a}(k)$ consisting of $(na + nb - 1)$ vector states as follows:

$$\boldsymbol{x_a}(k) = [y_a(k-1), \ldots, y_a(k-na), u(k-1), \ldots, u(k-nb+1)]^{\mathrm{T}}. \tag{4.2}$$

The state-space form of the discrete-time aerodynamic model is as follows:

$$\left.\begin{aligned} \boldsymbol{x_a}(k+1) &= \tilde{\boldsymbol{A}}_{\boldsymbol{a}}\boldsymbol{x_a}(k) + \tilde{\boldsymbol{B}}_{\boldsymbol{a}}u(k) \\ y_a(k) &= \tilde{\boldsymbol{C}}_{\boldsymbol{a}}\boldsymbol{x_a}(k) + \tilde{\boldsymbol{D}}_{\boldsymbol{a}}u(k), \end{aligned}\right\} \tag{4.3}$$

where:

$$\left.\begin{aligned}\tilde{\boldsymbol{A}}_a &= \begin{bmatrix} A_1 & A_2 & \cdots & A_{na-1} & A_{na} & B_1 & B_2 & \cdots & B_{nb-2} & B_{nb-1} \\ 1 & 0 & \cdots & 0 & 0 & 0 & 0 & \cdots & 0 & 0 \\ \vdots & 1 & \cdots & 0 & 0 & 0 & 0 & \cdots & 0 & 0 \\ \vdots & \vdots & \ddots & \vdots & \vdots & \vdots & \vdots & \ddots & \vdots & \vdots \\ 0 & 0 & \cdots & 1 & 0 & 0 & 0 & \cdots & 0 & 0 \\ 0 & 0 & \cdots & 0 & 0 & 0 & 0 & \cdots & 0 & 0 \\ 0 & 0 & \cdots & 0 & 0 & 1 & 0 & \cdots & 0 & 0 \\ 0 & 0 & \cdots & 0 & 0 & 0 & 1 & \cdots & 0 & 0 \\ \vdots & \vdots & \ddots & \vdots & \vdots & \vdots & \vdots & \ddots & \vdots & \vdots \\ 0 & 0 & \cdots & 0 & 0 & 0 & 0 & \cdots & 1 & 0 \end{bmatrix} \\ \tilde{\boldsymbol{B}}_a &= \begin{bmatrix} B_0 & 0 & 0 & \cdots & 0 & 1 & 0 & 0 & \cdots & 0 \end{bmatrix}^{\mathrm{T}} \\ \tilde{\boldsymbol{C}}_a &= \begin{bmatrix} A_1 & A_2 & \cdots & A_{na-1} & A_{na} & B_1 & B_2 & \cdots & B_{nb-2} & B_{nb-1} \end{bmatrix} \\ \tilde{\boldsymbol{D}}_a &= [B_0] \end{aligned}\right\} \tag{4.4}$$

To couple with the structural motion equation, the discrete-time state-space form equation is turned into the continuous-time form by bilinear transformation, and the model in the state-space form is constructed as (4.5):

$$\left.\begin{aligned}\dot{\boldsymbol{x}}_a(t) &= \boldsymbol{A}_a \boldsymbol{x}_a(t) + \boldsymbol{B}_a u(t) \\ y_a(t) &= \boldsymbol{C}_a \boldsymbol{x}_a(t) + \boldsymbol{D}_a u(t). \end{aligned}\right\} \tag{4.5}$$

As we construct the state-space model of the unsteady aerodynamics, the instability problem of the flow is converted into the analysis of eigenvalues of the matrix $\boldsymbol{A}_a$ in (4.5).

4.2. *Validation of the reduced-order model*

As discussed in § 3.1, there are two difficulties in constructing a linear ROM with external input in the unstable transonic buffet flow. Firstly, the ROM must be trained by appropriate signals based on the steady-state base flow. Different from the time-averaged flow, the steady-state base flow strictly satisfies the governing equations and boundary conditions in the mathematical form. It plays an important role in the modelling of unsteady flow and stability analysis (Dowell & Hall 2001; Barkley 2006; Illingworth, Morgans & Rowley 2012). For the symmetric cylinder wake flow, we can obtain the base flow by imposing a symmetric boundary condition or virtual damping (Zhang *et al.* 2015*c*). While for transonic buffet flow, the approach is to stabilize the unsteadiness by some control methods, which should not cause extra changes on the initial flow conditions such as the angle of attack, airfoil shape and so on. In our recent work (Gao *et al.* 2016*a*), the unstable steady-state solution of buffet flow is obtained by a closed-loop active control method. Under the optimal control law, the unsteadiness of the buffet flow is stabilized. The stabilized flow is the steady base flow for the given buffet state, which is used as the initial flow in the training process. Figure 5 shows pressure contours and streamlines of the time-averaged flow field and steady-state base flow field at $M = 0.7$, $\alpha = 5.5°$. By comparing pressure contours, significant differences are observed between the two flows. For the time-averaged flow, the shock wave disappears; while for the

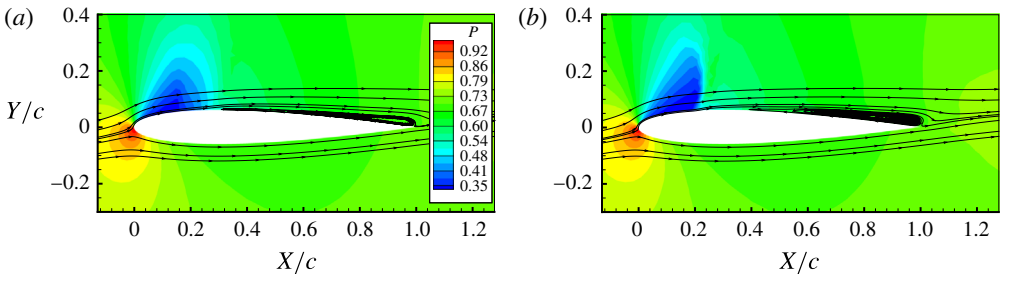

FIGURE 5. (Colour online) Pressure contours and streamlines of flow fields at $M = 0.7$, $\alpha = 5.5°$: (*a*) time-averaged flow; and (*b*) steady-state base flow.

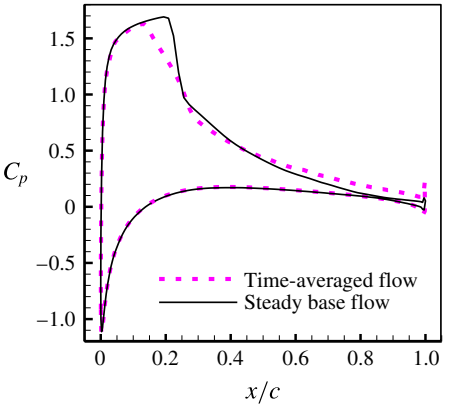

FIGURE 6. (Colour online) Comparison of pressure coefficients between the time-averaged flow and the steady-state base flow.

steady-state base flow, it remains at 20 % after the leading edge of the airfoil. This directly leads to the difference in the pressure coefficient, as shown in figure 6, and consequently to the difference in the aerodynamic force, as shown in figure 7(*a*), the pitching moment coefficient of the unstable steady base flow being slightly larger than that of the time-averaged one. Figure 7(*a*) also presents the evolution of the buffet flow at $M = 0.7$ and $\alpha = 5.5°$ based on the steady-state solution, and in figure 7(*b*), the response is plotted in the logarithm scale. When the non-dimensional time is less than 140, the amplitude of the moment coefficient is less than 0.015. At this stage, the evolution develops in an approximately linear way, which we define as the linear stage. When the non-dimensional time is larger than 140, the growing amplitude of the unstable aerodynamic force will ultimately give rise to a nonlinear, limit-cycling behaviour, which is certainly not linear. So the training process must be performed at the linear stage.

As to the second difficulty, the training signal must satisfy the following three requirements: (i) the frequency of the training signal should cover the buffet frequency; (ii) the amplitude of the training signal should be small, otherwise it will induce nonlinear responses; (iii) the training signal should not be too long and the training process must be finished before the amplitude of the moment reaches 0.015. As shown in figure 8(*a*), a chirp signal with an increasing frequency is designed as the input. Figure 8(*b*) shows the power spectrum density (PSD) analysis of the signal.

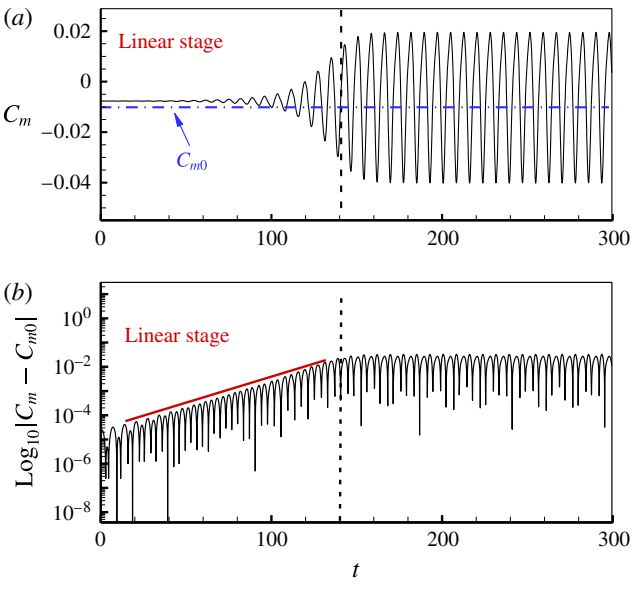

FIGURE 7. (Colour online) Evolution of the pitching moment coefficients based on the steady-state base flow are plotted in (*a*) normal scale and (*b*) logarithm scale, where C_{m0} indicates the mean pitching moment coefficient.

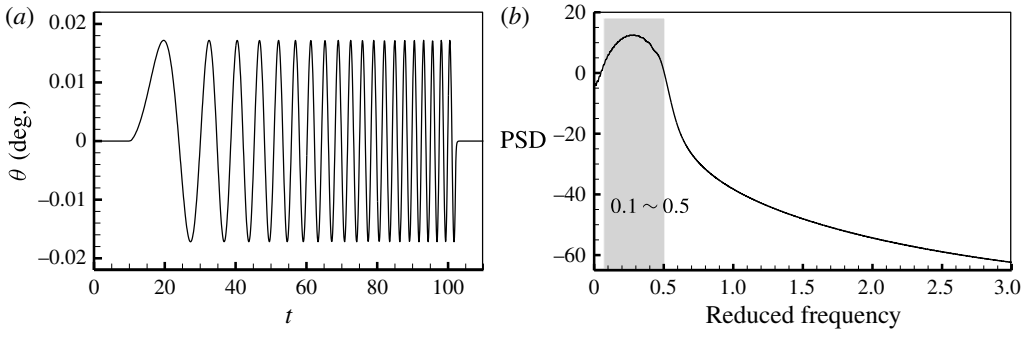

FIGURE 8. (*a*) Time history and (*b*) PSD analysis of the training signal.

Its dominant reduced frequencies are from 0.1 to 0.5, including the buffet reduced frequency. In addition, to reduce the impact of the airfoil sudden movement in the flow, a smoothing method with an average weight coefficient is used in the initial period of non-zero signals.

We set up the aerodynamic model at $M = 0.7$, $\alpha = 5.5°$ to verify the ROM. In order to accurately predict the unsteady aerodynamics, delay orders should be assigned with relatively large numbers, i.e. $na = nb = 80$. The identified results are compared with those of CFD simulations in figure 9; and a good agreement is observed between them. Therefore, the identification method based on the ARX model has a high numerical accuracy.

The ROM is then validated in the time domain by comparing with CFD simulations under the excitation of harmonic signals. The harmonic forcing signal is in the form of $\theta = \theta_{am} \sin(2\pi n f_b t)$. θ_{am} is the vibration amplitude of the airfoil; f_b is the frequency

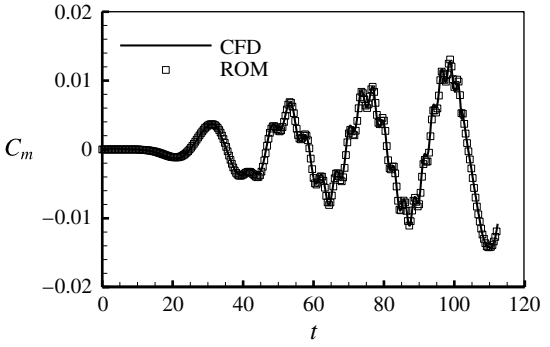

FIGURE 9. Identified results compared with those of CFD simulations.

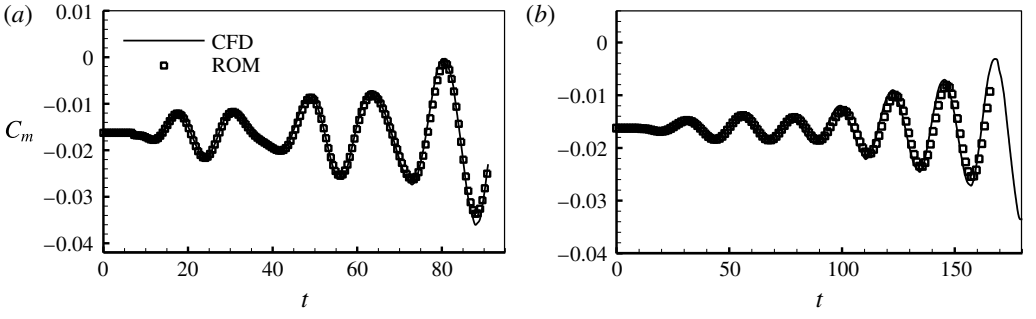

FIGURE 10. Comparisons of time responses of a harmonic pitching airfoil at $\alpha = 5.5°$ for (*a*) $\theta = 0.02\sin(1.4\pi f_b t)$ and (*b*) $\theta = 0.02\sin(2.6\pi f_b t)$.

of buffet; and n is the non-dimensional coefficient. Figure 10 shows comparison of time histories of the pitching moment coefficient between ROM and CFD simulation at two typical forcing frequencies ($n = 0.7$ and $n = 1.3$). ROM predictions exactly match those computed by the CFD simulation when the amplitude of the pitching moment coefficient is less than 0.015.

By solving the eigenvalue of matrix $\boldsymbol{A}_a$ in (4.5), we can obtain the least stable fluid mode, which is associated with the instability of the transonic buffet flow. The real part of the eigenvalue indicates the damping of the fluid mode, and a positive one means that the fluid is unstable. The imaginary part of the eigenvalue, in the reduced frequency scale, indicates the reduced frequency of the fluid mode. Figure 11 displays the trajectory of the least stable eigenvalue at $M = 0.7$, which changes smoothly as the angle of attack increases. The flow is globally stable (eigenvalues lie in the left half-plane) at small angles of attack up to $\alpha = 4.70°$. Then, the eigenvalue crosses the imaginary axis between $\alpha = 4.70°$ and $\alpha = 4.80°$. Note that the critical angle of the buffet onset obtained here corresponds to the angle computed by the CFD simulation, and it approximates to the $\alpha = 4.74°$ observed in the experiment by Doerffer *et al.* (2010). At $\alpha = 5.5°$, the buffet frequency from the present ROM is 0.196 and it is 0.198 from the CFD simulation (figure 4). This reveals that the linear buffet frequency by the ROM is almost the same as the nonlinear one by the CFD. Therefore, we will not differentiate them in the ensuing discussion, and they are both donated by k_b. This is different from the cylinder wake flow, in which the linear frequency is lower than

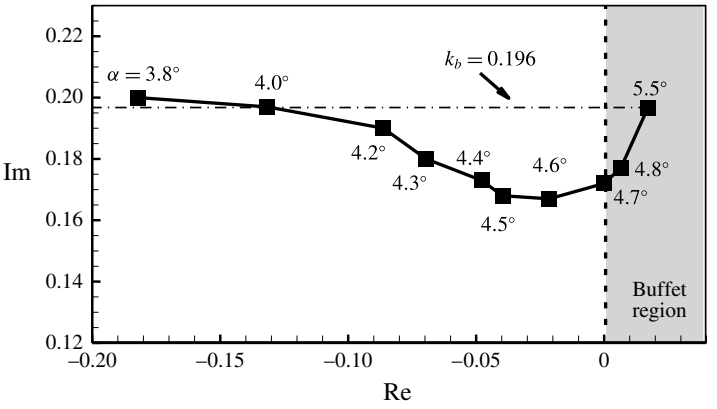

FIGURE 11. Least stable eigenvalues loci obtained by the ROM at various angles of attack at $M = 0.7$.

the nonlinear frequency (Zhang *et al.* 2015*c*), and in which the larger the Reynolds number is, the bigger the difference is (Sipp *et al.* 2010).

5. Models for aeroelasticity

5.1. *Coupled CFD/CSD simulation method*

The generalized structural motion equation in matrix form is as follows:

$$\boldsymbol{M}\cdot\ddot{\boldsymbol{\xi}} + \boldsymbol{G}\cdot\dot{\boldsymbol{\xi}} + \boldsymbol{K}\cdot\boldsymbol{\xi} = \boldsymbol{Q}, \tag{5.1}$$

where $\boldsymbol{\xi}$ is the structural generalized displacement; $\boldsymbol{M}$, $\boldsymbol{G}$ and $\boldsymbol{K}$ are the generalized mass, damping and stiffness matrices, respectively. $\boldsymbol{Q}$ is the generalized aerodynamic force provided by the CFD.

The structural motion equation can be non-dimensionalized by the time $\mathrm{d}t = U_\infty/b\,\mathrm{d}t_{physics}$. For the dynamics of the SDOF pitching airfoil with zero damping, equation (5.1) can be written as:

$$\ddot{\theta} + k_s^2\theta = \frac{1}{\pi\mu r_\alpha^2}(2C_m), \tag{5.2}$$

where θ represents the airfoil pitching angle. $k_s = \omega_s b/U_\infty$ is the reduced frequency non-dimensionalized by the half-aerodynamic chord b, natural frequency of the pitching spring ω_s and the free-stream velocity U_∞. Therefore, k_s represents the natural frequency of the elastic airfoil in the ensuing discussion. $\mu = m/\pi\rho b^2$ is the non-dimensional mass ratio, where m and ρ represent the mass of the wing with unit span and the density of the free stream, respectively. r_α is the gyration radius of the airfoil around the elastic axis at $a = 0.224c$. C_m is the pitching moment coefficient. A sketch diagram of the SDOF pitching airfoil is shown in figure 12.

By defining the structural state vector $\boldsymbol{x} = [\theta, \dot{\theta}]^{\mathrm{T}}$, the structural motion equation in the state-space form is as follows:

$$\dot{\boldsymbol{x}} = \boldsymbol{F}(\boldsymbol{x}, t) = \boldsymbol{A}\boldsymbol{x} + \boldsymbol{B}Q(C_m), \tag{5.3}$$

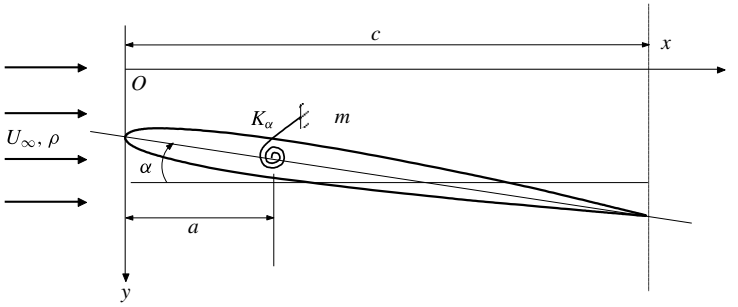

FIGURE 12. Sketch diagram of the SDOF pitching airfoil system.

where $\boldsymbol{A}=\begin{bmatrix}\boldsymbol{0} & \boldsymbol{I}\\ -\boldsymbol{M}^{-1}\boldsymbol{K} & -\boldsymbol{M}^{-1}\boldsymbol{G}\end{bmatrix}$; $\boldsymbol{B}=\begin{bmatrix}\boldsymbol{0}\\ \boldsymbol{M}^{-1}\end{bmatrix}$; $\boldsymbol{0}$ is the zero matrix; $\boldsymbol{I}$ is the identity matrix; and Q is a function of C_m, defined by $Q(C_m)=2C_m/(\pi\mu r_\alpha^2)$. Equation (5.3) is a first-order differential equation system. A fourth-order accuracy hybrid linear multi-step method (Zhang, Jiang & Ye 2007) is used to solve the aeroelastic equation (5.3) in the time domain.

Lack of a standard case for the SDOF flutter, the above-coupled CFD/CSD simulation method is validated by classical flutter cases with two degrees of freedom. In our previous work, flutter boundaries of the bench active control technology (BACT) model (Zhang *et al.* 2015*b*), the Isogai wing (Zhang *et al.* 2007) and the LCO with NACA64010 airfoil (Zhang *et al.* 2012) agreed well with experimental data and reference results.

5.2. *ROM-based aeroelastic model*

Defining the structural state vector $\boldsymbol{x}_s=[\theta,\dot{\theta}]^{\mathrm{T}}$ for the present SDOF pitching airfoil, the structural motion equation (5.1) in the state-space form can be rewritten as:

$$\left.\begin{aligned}\dot{\boldsymbol{x}}_s(t)&=\boldsymbol{A}_s\boldsymbol{x}_s(t)+q\boldsymbol{B}_s y_a(t)\\ u(t)&=\boldsymbol{C}_s\boldsymbol{x}_s(t)+q\boldsymbol{D}_s y_a(t),\end{aligned}\right\} \tag{5.4}$$

where $\boldsymbol{A}_s=\begin{bmatrix}0 & 1\\ -k_s^2 & 0\end{bmatrix}$, $\boldsymbol{B}_s=\begin{bmatrix}0\\ 1\end{bmatrix}$, $\boldsymbol{C}_s=\begin{bmatrix}1 & 0\end{bmatrix}$, $\boldsymbol{D}_s=[0]$, $q=1/(\pi\mu r_\alpha^2)$.

By defining the state vector $\boldsymbol{x}_{ae}=[\boldsymbol{x}_s,\boldsymbol{x}_a]^{\mathrm{T}}$ and coupling the structural state equations (5.4) with the aerodynamic state equations (4.5), we obtain the state equation and output equation for the linear aeroelastic system as follows:

$$\left.\begin{aligned}\dot{\boldsymbol{x}}_{ae}(t)&=\begin{bmatrix}\boldsymbol{A}_s+q\cdot\boldsymbol{B}_s\boldsymbol{D}_a\boldsymbol{C}_s & q\cdot\boldsymbol{B}_s\boldsymbol{C}_a\\ \boldsymbol{B}_a\boldsymbol{C}_s & \boldsymbol{A}_a\end{bmatrix}\cdot\boldsymbol{x}_{ae}(t)=\boldsymbol{A}_{ae}\cdot\boldsymbol{x}_{ae}(t)\\ u(t)&=\begin{bmatrix}\boldsymbol{C}_s & 0\end{bmatrix}\cdot\boldsymbol{x}_{ae}(t).\end{aligned}\right\} \tag{5.5}$$

The ROM-based aeroelastic model of a SDOF pitching airfoil system is then obtained. The problem of aeroelastic stability is converted into the analysis of complex eigenvalues of $\boldsymbol{A}_{ae}$. The process of the transonic aeroelastic analysis is:

(i) Use the URANS flow solver to compute the aerodynamic coefficient of the mode with the designed input signal in figure 8.

(ii) Use the identification technique to construct the input–output difference model (4.3) in the discrete-time domain, and then turn it into the continuous-time state-space form (4.5).

(iii) Couple the aerodynamic state-space equation (4.5) and the structural state-space equation (5.4) to obtain the ROM-based aeroelastic state-space equation (5.5).

(iv) Solve the complex eigenvalues of the state matrix $\boldsymbol{A}_{ae}$ in (5.5). We focus on the two most unstable eigenvalues, which correspond to the fluid and structural modes. With different structural parameters, natural frequencies of the elastic airfoil and mass ratios, we can obtain a set of eigenvalues. It is the root loci. The stability of the aeroelastic system changes when the root loci cross the imaginary axis.

The model is then validated by the BACT case (Rivera *et al.* 1992). Although this case is a two DOF system, procedures for the modelling are the same. Therefore, it is an alternative validation owing to lack of standard cases for the SDOF system. The results are shown in appendix C.

6. Results and discussion

This paper focuses on the frequency lock-in phenomenon in transonic buffeting flows. An NACA 0012 airfoil at $M = 0.7$, $\alpha = 5.5°$ and $Re = 3 \times 10^6$ is used as the computational case. The ROM-based aeroelastic model constructed in § 5.2 is applied to analyse the mechanism of the phenomenon. The coupled CFD/CSD method constructed in § 5.1 is used as a supplement to conclusions from the ROM-based aeroelastic model. The airfoil is free to vibrate in SDOF pitching with a supporting axis at $0.224c$. In § 6.1, the frequency lock-in phenomenon is simulated based on the coupled CFD/CSD method. In § 6.2, eigenvalue analysis of the ROM-based aeroelastic model is conducted, and the mechanism underlying the lock-in is discussed. In § 6.3, the effect of the mass ratio μ is investigated. But before further discussion, some frequencies should be clarified. The first is k_b, which is the buffet frequency of the rigid airfoil as discussed in § 4.2. The second is k_s, which is the natural frequency of the elastic airfoil. And the last is k_{ae}, which is the coupling frequency of the aeroelastic system.

6.1. *Characteristics of the frequency lock-in*

Figures 13–15 show time history responses and PSD analyses at different natural frequencies (k_s) of the elastic airfoil at $\mu = 200$. In the cases of $k_s = 0.10$ (figure 13) and $k_s = 0.60$ (figure 14), the amplitudes of the pitching angle responses are very small; and the amplitudes of the pitching moment coefficient are approximately equal to those of the rigid model (figure 7). PSD analyses show that coupling frequencies (k_{ae}) are dominated by the buffet frequency ($k_b = 0.196$), which displays forced vibration under the unstable buffet loads. However, in the case of $k_s = 0.35$ (figure 15), the basic coupling frequency is no longer dominated by the buffet frequency, but follows the natural frequency of the elastic airfoil. This is the frequency lock-in phenomenon. When it occurs, the amplitude of the oscillating pitching angle exceeds 8°, and the amplitude of the moment coefficient is much larger than that of the rigid model. Such large-amplitude oscillations may cause serious flight accidents.

Furthermore, figure 16 shows the coupling frequency (k_{ae}) of the aeroelastic system as a function of the natural frequency (k_s). In most regions, the coupling frequency follows the buffet frequency. However, in the region of $0.21 < k_s < 0.46$ (the lower boundary is controversial, which will be discussed in next section), the coupling frequency locks onto the natural frequency. The dashed line $k_{ae} = k_s$ represents the lock-in phenomenon. It is found that lock-in can occur in a wider range at the ratio

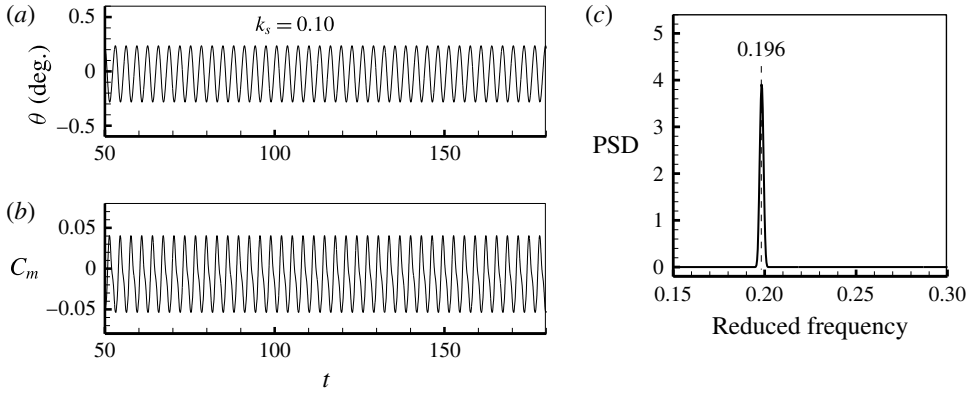

FIGURE 13. Time histories at $k_s = 0.10$ of (*a*) the pitching angle response; (*b*) the pitching moment coefficient response; and (*c*) the PSD analysis of the pitching moment coefficient response.

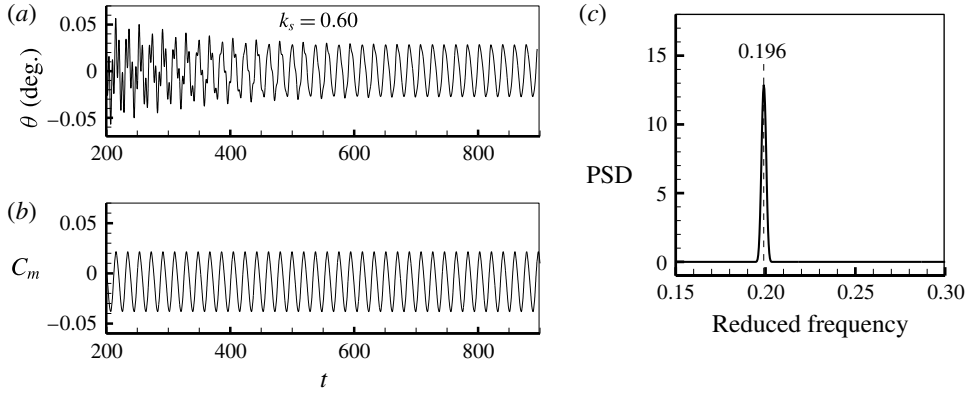

FIGURE 14. Time histories at $k_s = 0.60$ of (*a*) the pitching angle response; (*b*) the pitching moment coefficient response; and (*c*) the PSD analysis of the pitching moment coefficient response.

of natural frequency to buffet frequency (k_s/k_b) from 1.07 to 2.34. Previous research attributed the frequency lock-in to resonance. However, the so-called 'resonance region' ($0.21 < k_s < 0.46$ or $1.07 < k_s/k_b < 2.34$) does not display a symmetrical distribution against the buffet frequency (0.196), but it is entirely located in the higher frequency side. Is frequency lock-in in transonic buffeting flow really caused by resonance?

6.2. *Mechanism of the frequency lock-in*

The mechanism underlying the lock-in will be discussed in this section using the ROM-based aeroelastic model. Figure 17 presents the eigenvalue loci of the coupled system varying with the natural frequency (k_s) of the airfoil at $\mu = 200$. It can be found that the eigenvalue loci have two branches, which we define as branch A and branch B. For branch A, its mode is stable (eigenvalues lie in the left half-plane)

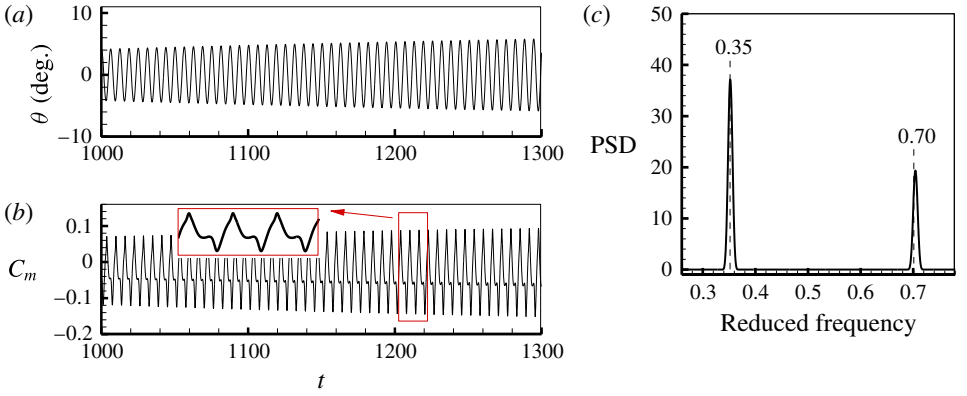

FIGURE 15. (Colour online) Time histories at $k_s = 0.35$ of (*a*) the pitching angle response; (*b*) the pitching moment coefficient response; and (*c*) the PSD analysis of the pitching moment coefficient response.

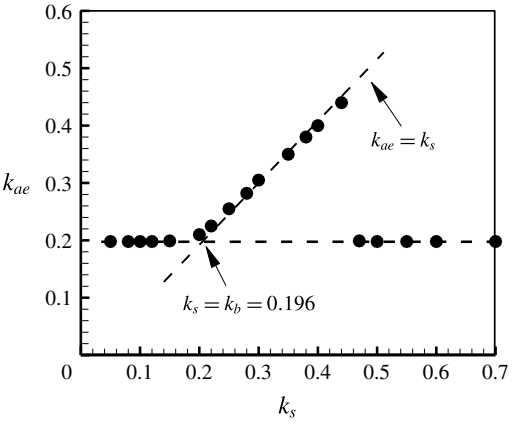

FIGURE 16. Oscillating frequency of the aeroelastic system as a function of the natural frequency of the elastic airfoil.

at low natural frequencies; then as the natural frequency increases, it crosses into the right half-plane, and the coupling frequency of the system at the crossing point is $k_{ae} = 0.196$; as the natural frequency increases furthermore, it approaches the uncoupled least stable fluid mode (refer to figure 11 at $\alpha = 5.5°$). However, for branch B, it is unstable at the initial stage; then as the increase of the natural frequency, it crosses into the left half-plane, and the coupling frequency at the crossing point is $k_{ae} = 0.46$.

Figure 18 shows the imaginary part of the eigenvalue loci in figure 17 as a function of the natural frequency k_s. At low natural frequencies, the coupling frequency of branch A follows the natural frequency of the structural model (S mode); and the coupling frequency of branch B is dominated by the buffet frequency of the fluid mode (F mode). However, at high natural frequencies, the coupling frequency of branch A turns to be dominated by the buffet frequency; while that of branch B becomes to follow the natural frequency. The corresponding modes also exchange.

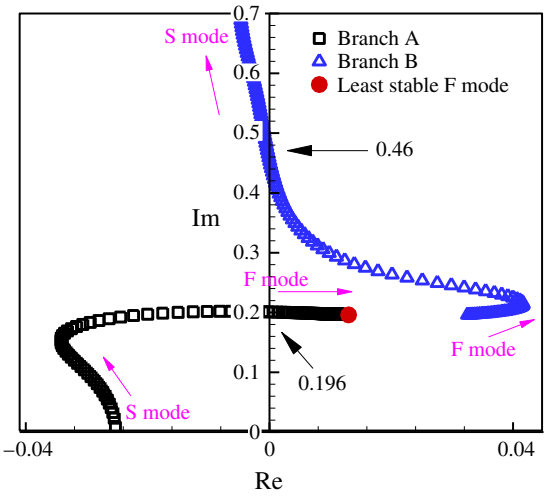

FIGURE 17. (Colour online) Eigenvalue loci of the aeroelastic system at $M = 0.7$, $\alpha = 5.5°$ and $\mu = 200$.

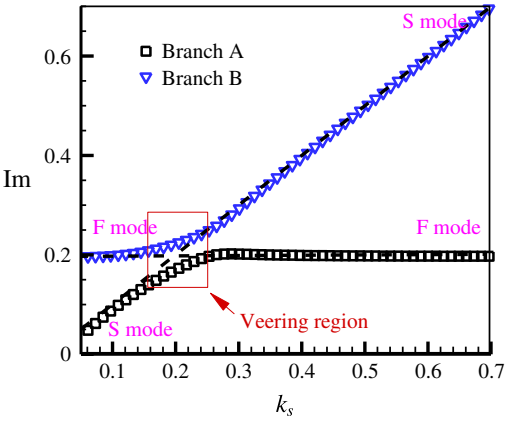

FIGURE 18. (Colour online) Imaginary part of the eigenvalue loci as a function of the natural frequency.

From the above analysis, it can be seen that there is mode veering between the two branches. Mode veering refers to the phenomenon associated with the imaginary part (frequency) of the eigenvalue loci of a system with a variable parameter: two branches approach each other and then veer away and diverge instead of intersecting (Perkins & Mote 1986; Chen & Kareem 2003; Vijayann & Woodhouse 2014). When mode veering occurs, eigenmodes (eigenvectors) associated with these two branches also exchange in a continuous way. Meliga & Chomaz (2011) first found the veering phenomenon between F mode and S mode, which was defined as mode transition in their study, when they investigated the effect of mass ratio on the instability of a spring mounted circular cylinder. It is found that if the mass ratio is larger than the critical mass ratio, the instability is led by F mode; if it is smaller, the instability is led by S mode; and if it is close to the critical mass ratio, no clear distinction can be found between the two modes.

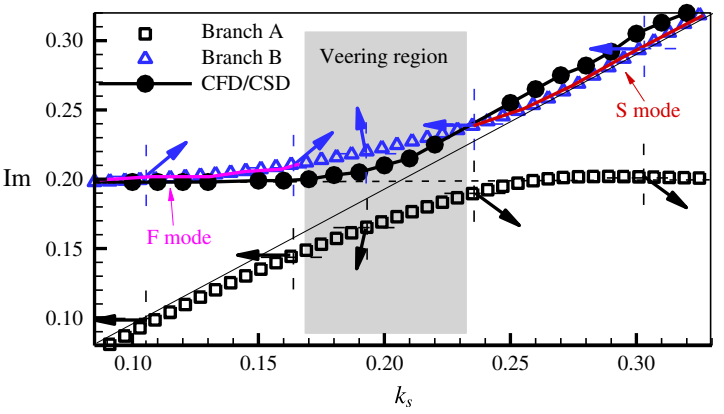

FIGURE 19. (Colour online) Mode veering of imaginary part (frequency) of the eigenvalue loci with the varying natural frequency of the elastic airfoil. The blue triangle symbol refers to branch B, and the black square symbol refers to branch A. The dashed line denotes the buffet frequency of the rigid airfoil, and the solid line denotes the natural frequency. Blue arrows denote directions of eigenvectors associated with branch B, and black arrows denote those of branch A. The grey area refers to the mode veering region based on the approximate law.

Figure 19 shows the close-up view of the veering region, as well as the coupling frequency of the aeroelastic system from the coupled CFD/CSD simulation which corresponds to that of branch B. As the natural frequency (k_s) of the elastic airfoil approaches to the buffet frequency (k_b), the loci of branch A and branch B tend to veer and march along each other's previous locus (dashed and solid lines in figure 19), thus avoiding an intersection; and the modes associated with these two frequencies exchange. We also plot the directions (the real part and the imaginary part in complex plane) of the complex eigenvectors. As shown in figure 19, only components of interest are displayed, black and blue arrows standing for branch A and branch B, respectively. The directions also exchange after the mode veering. Therefore, they can be used to track the mode veering region. A common approximate law is defined as: if the direction of an eigenvector displays a deflection more than 10° compared with that of the initial (last) one, we define it as the onset (offset) of the veering region. Based on this law, the mode veering region (the grey area), $0.168 < k_s < 0.232$ or $0.83 < k_s/k_b < 1.18$, can be marked in figure 19. Therefore, we can draw a panorama of the mode veering associated with branch B with the increasing natural frequency. Before the mode veering, $k_s < 0.168$, branch B corresponds to F mode; while after that, $k_s > 0.232$, it turns to correspond to S mode. In the veering region, $0.168 > k_s > 0.232$, the mode property of branch B transforms from F to S. Due to the continuity of the transformation, it is difficult to distinguish S mode from F mode in the region.

Figure 20 shows the real part (represents the damping characteristics) and imaginary part (represents the frequency characteristics) of the eigenvalue loci in figure 17, as well as the coupling frequency and the amplitude of the pitching angle from the coupled CFD/CSD simulation as functions of the natural frequency of the elastic airfoil. Since the real part and the imaginary part share the same veering range, the real part also displays the mode veering phenomenon (figure 20*b*), which has been discussed in the imaginary part of the loci in figure 19. Before the veering

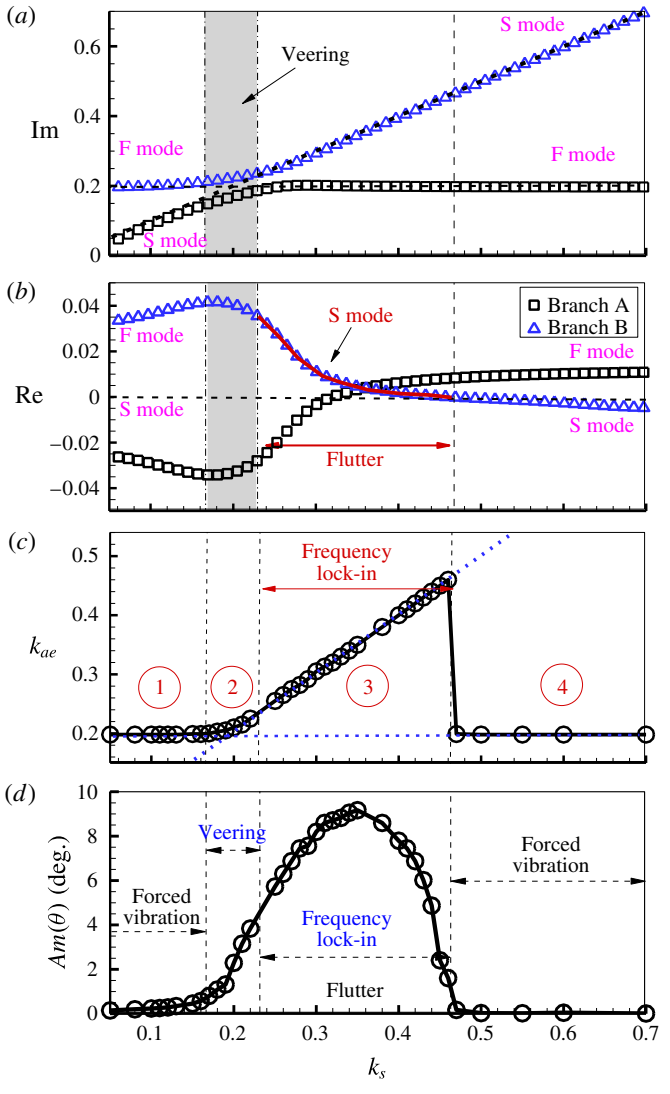

FIGURE 20. (Colour online) (*a*) Imaginary part of the eigenvalue loci, (*b*) real part of the eigenvalue loci from the ROM-based aeroelastic model; and (*c*) coupling frequency of the system, (*d*) oscillating amplitude of the pitching airfoil from the coupled CFD/CSD simulation varying with the natural frequency of the elastic airfoil.

($k_s < 0.168$), branch B stands for F mode, but after that ($k_s > 0.232$), it turns to stand for S mode. From figure 20(*b*), it can also be seen that the damping (real part) of S mode is positive at $0.232 < k_s < 0.460$. Based on the linear eigenvalue theory, a positive damping means the instability of S mode, namely, flutter in aeroelasticity. The upper flutter boundary (the crossing point) is at $k_s = 0.460$, which is exactly equal to the upper boundary of the lock-in region from the coupled CFD/CSD simulation.

Figure 21 shows the comparison of the logarithmic increment of the pitching angle between the coupled CFD/CSD simulation and the ROM-based aeroelastic model. The logarithmic increment from the ROM-based model is transformed

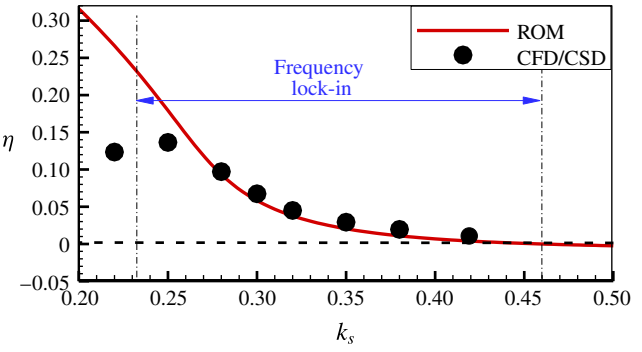

FIGURE 21. (Colour online) Comparison of the logarithmic increment between the coupled CFD/CSD simulation and the ROM-based aeroelastic model as a function of the natural frequency of the elastic airfoil.

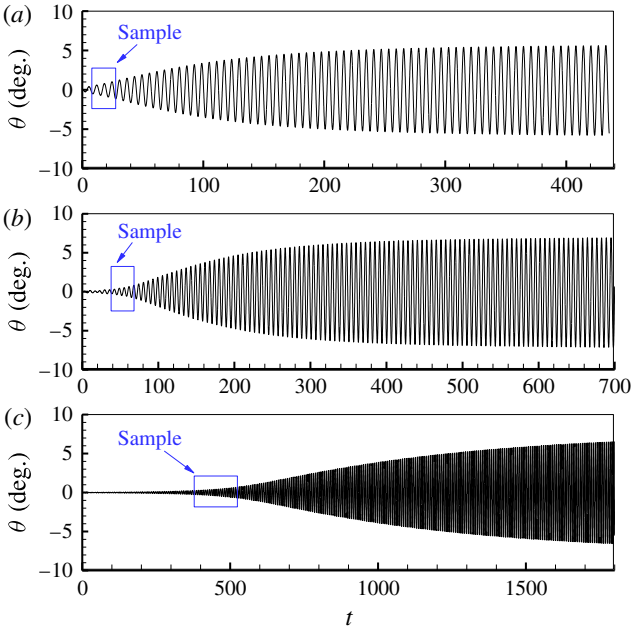

FIGURE 22. (Colour online) Time history of the pitching angle of the airfoil from the coupled CFD/CSD simulation and the sample for the calculation of the logarithmic increment at (*a*) $k_s = 0.25$, (*b*) $k_s = 0.28$ and (*c*) $k_s = 0.42$.

from the real part (positive damping) of branch B in figure 20(*b*). In the coupled CFD/CSD simulation, it is calculated from the time history of the pitching angle at the initial stage with approximately exponential oscillation. It is defined as $\eta = Ln(Am^{j+1}(\theta) - Am^{j}(\theta))/Am^{j}(\theta)$, where $Am^{j}(\theta)$ represents the amplitude of the jth cycle. Responses and samples for the calculation of the logarithmic increment at typical natural frequencies are shown in figure 22. It can be seen that the logarithmic increment from the coupled CFD/CSD simulation can reasonably match that predicted by the linear model. As shown in figure 22(*a*), at $k_s = 0.25$, the oscillation reaches a

LCO rapidly because of the higher linear increment (positive damping). In this case, the nonlinearity dominates the system. The predicted increment from the sample of the simulation is also dominated by the nonlinearity. Therefore, errors at cases of $k_s < 0.25$ are reasonable. In the case of $k_s = 0.42$, the time history of the pitching angle displays an exponential growth. Both logarithmic increments are in good agreement. Therefore, from the results in figures 19 and 21, both are convincing, the characteristics of the frequency and the damping in the lock-in region predicted by the linear ROM-based aeroelastic model. Besides, the frequency lock-in is dominated by linear dynamics.

In order to thoroughly understand the dynamics of the buffeting response, the natural frequency (k_s) of the airfoil is divided into four sub-regions, as shown in figure 20(*c*). They are divided by three critical natural frequencies, namely, the lower and upper boundaries ($k_s^l = 0.168$, $k_s^m = 0.232$) of the frequency loci veering, and the upper flutter boundary ($k_s^u = 0.460$). In sub-regions 1 ($k_s < 0.168$) and 4 ($k_s > 0.460$), coupling frequencies follow the buffet frequency, namely, $k_{ae} = k_b$. In fact, they are both forced vibration caused by the unsteady buffeting loads. Vibration amplitudes of the airfoil are comparatively small in these two sub-regions. In sub-region 2 ($0.168 < k_s < 0.232$), namely, the mode veering region, the coupling frequency neither follows the buffet frequency nor the natural frequency. The oscillating amplitude of the airfoil in this sub-region is between that in sub-regions 1 and 3. It is a transitional stage. However, due to the continuity of the veering process, it is hard to identify which mode, S mode or F mode, dominates the system instability. In sub-region 3 ($0.232 < k_s < 0.460$), the coupling frequency synchronizes with the natural frequency ($k_{ae} = k_s$) – the phenomenon of the frequency lock-in, and the airfoil vibrates with an increasing amplitude. The peak oscillation amplitude is achieved at a distinctly high frequency ratio of $k_s/k_b = 1.73$ rather than $k_s/k_b = 1.0$.

Results from the above discussion indicate that the coupling between the S mode and F mode leads to the instability of the former. Besides, the instability range coincides with the lock-in region obtained from the coupled CFD/CSD simulation. It reveals that the frequency lock-in is caused by the linear coupled-mode flutter. However, the flutter in this study is not a classical mode coupling between structural modes but a coupling between one structural mode and one fluid mode. Therefore, the physical mechanism underlying the frequency lock-in phenomenon in transonic buffeting flow is SDOF flutter. But different from the classical SDOF flutter (e.g. transonic buzz) which occurs from an initial stable flow, the present one is in the unstable buffeting flow. Its particularity is the competition between two unstable modes. Therefore, the response of the airfoil system undergoes a conversion from the forced vibration to the self-sustained oscillation (flutter). The coupling frequency certainly should lock onto the natural frequency of the elastic airfoil. The occurrence of the frequency lock-in is dominated by the linear dynamics.

The conversion is then validated by the coupled CFD/CSD simulation at $\mu = 200$ and $k_s = 0.3$ with zero initial condition of the displacement and velocity. Based on the analysis of the linear dynamics, there are two unstable modes in this case, F mode and S mode. The complex response can be explained by the competition between the two unstable modes. Figure 23 shows the time history and the frequency content of the responses. The response history can be divided into three stages. In the first stage, $t < 200$, the pitching angle is very small and the pitching moment coefficient vibrates with the amplitude approximately equal to that of the rigid airfoil. The coupling frequency is followed by the buffet frequency ($k_b = 0.196$) (figure 23*c*). Therefore,

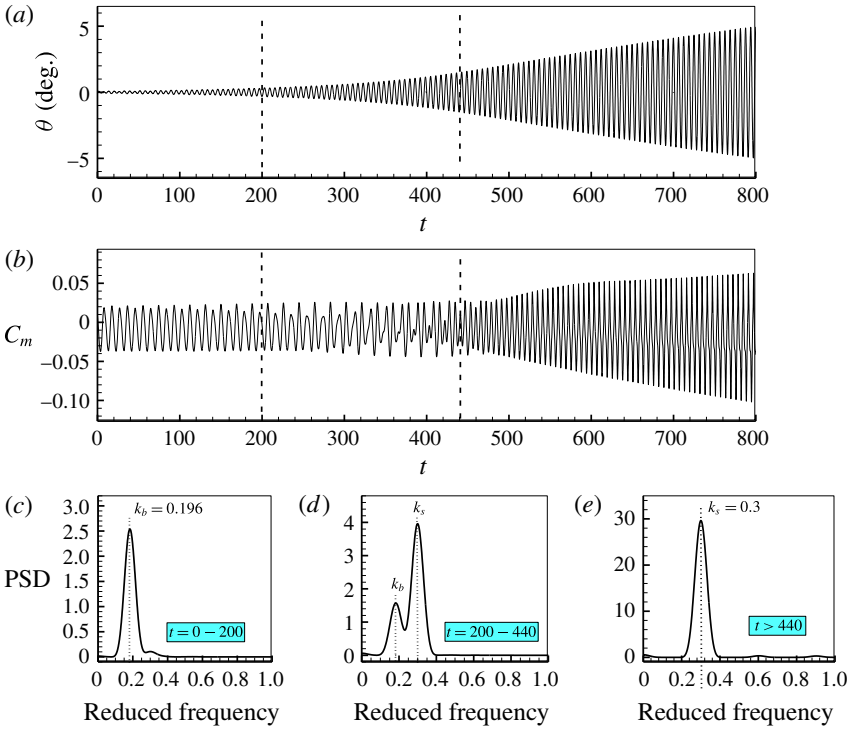

FIGURE 23. (Colour online) Time history of (*a*) the pitching angle, (*b*) the pitching moment coefficient and (*c–e*) frequency contents of the aeroelastic system at $M = 0.7$, $\alpha = 5.5°$ and $\mu = 200$, $k_s = 0.3$ with zero initial conditions.

the system is dominated by the unstable F mode, displaying forced vibration under the unstable buffet loads in this stage. In the second stage, $200 < t < 440$, there are two peak frequency components, the buffet frequency with less power, and the natural frequency with more power (figure 23*d*). It means that, as the response time goes, the buffet frequency becomes weak, while the natural frequency becomes strong. That is, the unstable S mode gradually dominates the dynamic characteristics of the system. Finally, in the last stage, $t > 440$, the responses diverge. The oscillating frequency absolutely follows the natural frequency (figure 23*e*). The frequency lock-in phenomenon occurs. The unstable S mode completely dominates the characteristics of the system. Therefore, the system in this stage displays self-sustained oscillations (flutter).

With time going on ($t > 800$), responses of the pitching angle and the moment coefficient increase rapidly and eventually approach LCOs. Owing to a limited time range, LCO is not shown in figure 23, but it is exhibited in figure 15. It can be seen that the pitching moment does not display a simple harmonic response (figure 15*b*). The PSD result shows two peaks (figure 15*c*). The basic peak (0.35) is accurately located at the structural reduced frequency, and the second one equals twice that of the structural reduced frequency. This is a nonlinear response. We notice that the airfoil pitching angle exceeds 8° (figure 15*a*). Such a large-amplitude pitching motion certainly leads to a nonlinear flow, and consequently results in a double frequency response of the pitching moment. However, we want to specifically emphasize that

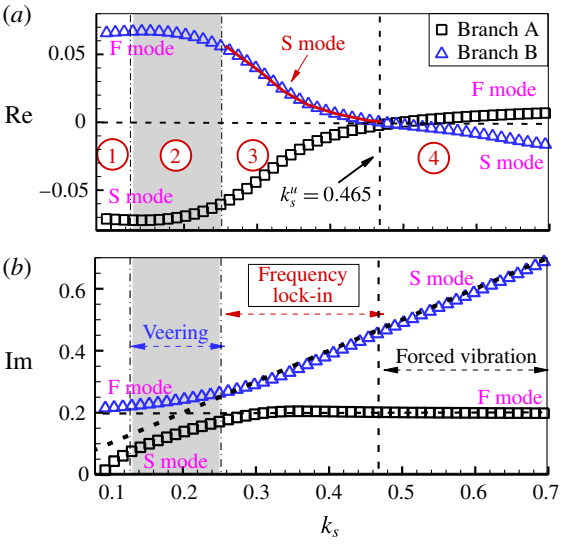

FIGURE 24. (Colour online) (*a*) Real part and (*b*) imaginary part of the eigenvalue loci at $\mu = 60$ as functions of the natural frequency of the elastic airfoil.

the nonlinearity dominates the system only when the structural pitching angle is large enough. At the initial stage of the response with a small pitching angle, the system is dominated by the instability of the structural mode (flutter). In transonic flow, a divergent response (flutter) generally reaches a LCO finally, as a result of the shock wave. Therefore, the nonlinear response (LCO) is just the final performance of the coupling linear flutter.

Some researchers have investigated the frequency lock-in in unstable flows with harmonic forcing, such as the transonic buffet flow by Raveh & Dowell (2011) and the open-cavity flow by Sipp (2012). These studies used uncoupled methods, and in particular, the lock-in range depends on the forcing amplitude. In essence, there exists a completion between the unstable flow and the unsteadiness caused by the forcing. As long as the forcing amplitude is large enough, the unsteadiness of the forcing flow will dominate the entire characteristics of the system.

6.3. *Effect of the mass ratio*

The investigation in §§ 6.1 and 6.2 is performed at a fixed mass ratio $\mu = 200$. This section will focus on the effect of the mass ratio on the dynamics of the buffeting response and frequency lock-in.

Figures 24 and 25 show the complex eigenvalue loci as functions of the natural frequency (k_s) of the elastic airfoil at $\mu = 60$ and $\mu = 1000$, respectively. Generally, the analysis procedure is similar to that of the eigenvalue loci at $\mu = 200$. We first recognize properties of the two branches and boundaries of the veering region by directions of eigenvectors based on the imaginary part of the eigenvalue loci (figures 24*b* and 25*b*). Then, we determine the upper flutter boundary (the crossing point of branch B) in the real part of the eigenvalue loci (figures 24*a* and 25*a*). Therefore, we can get three critical frequencies, the lower and upper boundaries (k_s^l and k_s^m) of the veering region and the upper flutter boundary (k_s^u). In the case of $\mu = 60$,

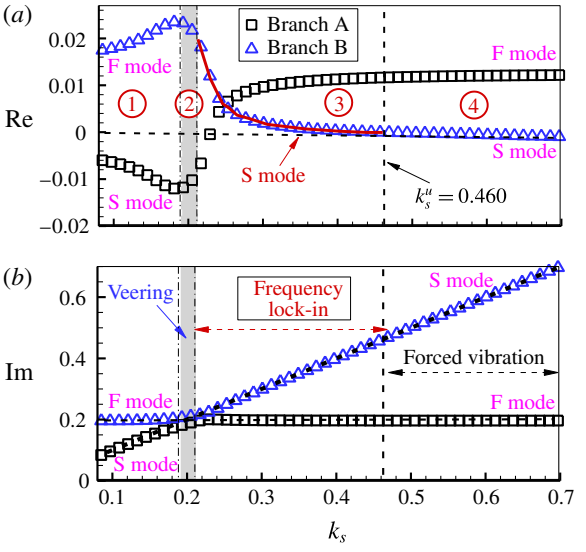

FIGURE 25. (Colour online) (*a*) Real part and (*b*) imaginary part of the eigenvalue loci at $\mu = 1000$ as functions of the natural frequency of the elastic airfoil.

$k_s^l = 0.126$, $k_s^m = 0.253$ and $k_s^u = 0.460$; while in the case of $\mu = 1000$, $k_s^l = 0.190$, $k_s^m = 0.210$ and $k_s^u = 0.460$. According to the three critical points, the natural frequency can be also divided into four sub-regions, namely, the forced vibration regions as sub-region 1 and 4, the mode veering region as sub-region 2 and the frequency lock-in region as sub-region 3. As discussed in § 5.2, the responses are forced vibrations in sub-regions 1 and 4 with smaller oscillating amplitudes, and the coupling frequencies always follow the buffet frequency. In sub-region 3, S mode is unstable, and the unstable region coincides with the lock-in region. It provides further evidence for the fact that the frequency lock-in phenomenon in transonic buffeting flow is caused by the linear coupled flutter. Furthermore, we notice that the upper flutter boundary (the crossing point, k_s^u) is substantially fixed at $k_s^u = 0.460$ at different mass ratios. This reveals that the mass ratio has a slight influence on this boundary. This is different from the conclusion in VIV (Meliga & Chomaz 2011; Zhang *et al.* 2015*c*), in which the upper boundary of the lock-in is significantly affected by the mass ratio, especially when the mass ratio is rather small. In sub-region 2, veering boundaries greatly rely on the mass ratio. The veering range changes from (0.126, 0.253) to (0.190, 0.210) as the mass ratio increases from $\mu = 60$ to $\mu = 1000$. Thus, the larger the mass ratio is, the narrower the veering region is and the closer veering boundaries are to the buffet frequency.

Figure 26 shows the comparison of the coupling frequency (k_{ae}) between the coupled CFD/CSD simulation and the ROM-based aeroelastic model at both mass ratios. The coupling frequency obtained by the simulation reasonably matches that of the model. Especially, the linear ROM-based aeroelastic model can accurately predict the upper flutter boundary. Therefore, it further proves that the frequency lock-in in transonic buffeting flow is dominated by linear dynamics. However, the characteristics of veering, to a certain extent, are associated with nonlinear dynamics when the mass ratio is small. In this region, the interaction between fluid and structure is strong, and the linear stage is very short, which is believed to be responsible for the gap

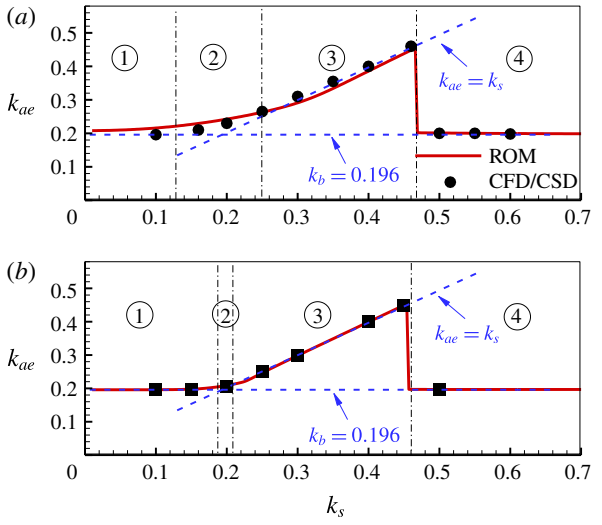

FIGURE 26. (Colour online) Comparison of the coupling frequency between the ROM-based aeroelastic model and CFD/CSD simulation at (*a*) $\mu = 60$ and (*b*) $\mu = 1000$.

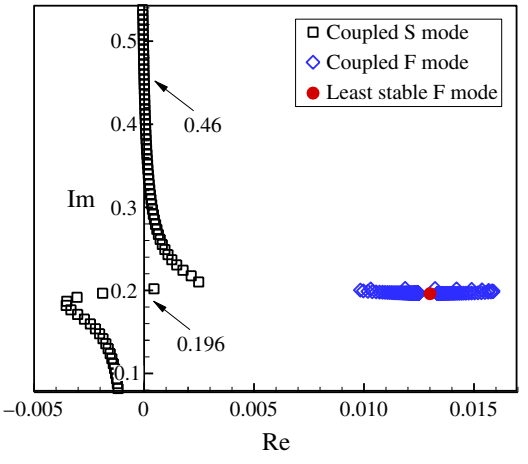

FIGURE 27. (Colour online) Eigenvalue loci of the coupled system at $M = 0.7$, $\alpha = 5.5°$ and $\mu = 5000$.

between the linear model and the nonlinear coupled CFD/CSD simulation at $\mu = 60$. A full weakly nonlinear model, such as that reported by Meliga & Chomaz (2011), may help to analyse cases with very small mass ratios.

We further enlarge the mass ratio to $\mu = 5000$. The eigenvalue loci are shown in figure 27. It can be seen that the loci display two separated and clean clusters. One fluctuates in the vicinity of the least stable F mode (figure 11), and forms a circle with the increasing natural frequency (k_s) of the elastic airfoil. The other fluctuates in the vicinity of the imaginary axis, first crossing the axis from the left half-plane to the right half-plane at $k_s = 0.196$ and then crossing from the right to the left at $k_s = 0.460$. This is different from the eigenvalue loci in figure 17.

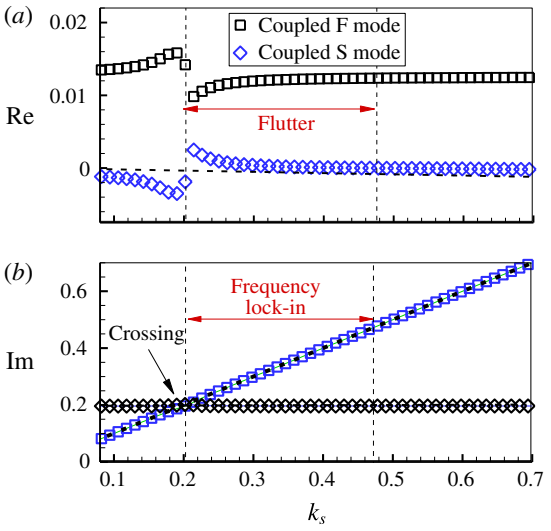

FIGURE 28. (Colour online) (*a*) Real part of the eigenvalue loci and (*b*) imaginary part of the eigenvalue loci as functions of the natural frequency of the elastic airfoil at $M = 0.7$, $\alpha = 5.5°$ and $\mu = 5000$.

In this case, $\mu = 5000$, the branch in the vicinity of the least stable F mode is a coupled F mode. And the other branch near the imaginary axis is a coupled S mode. Figure 28 shows the real and imaginary parts of complex eigenvalue as functions of the natural frequency of the elastic airfoil. From the imaginary part in figure 28(*b*), it can be seen that the coupled-mode frequencies always follow their uncoupled frequencies. When $k_s = 0.196$, the two loci intersect but do not repeal. This is the phenomenon of loci crossing. Different from the loci veering, eigenmodes associated with the two branches do not exchange in loci crossing. As shown in figure 28(*a*), the damping of S mode is positive when the natural frequency is within the range of $0.196 < k_s < 0.460$, indicating the instability of S mode (flutter). This range is also the lock-in region from the coupled CFD/CSD simulation. This further verifies that the frequency lock-in in transonic buffeting flow is caused by the linear coupled-mode flutter.

It can be seen that with the increase of the mass ratio, the imaginary part (frequency) of the eigenvalue loci changes from veering to crossing, which suggests the existence of a critical mass ratio. It is closely related to characteristics of the least stable F mode. That is, free-stream parameters, namely, Mach number, angle of attack and Reynolds number determine the critical mass ratio. In the present study, we calculate that the critical mass ratio is $\mu = 3350$. Figure 29 shows the mode veering region and the frequency lock-in region at different mass ratios. Good agreement is observed between boundaries calculated by the coupled CFD/CSD simulation and those obtained by the ROM-based aeroelastic model. As the mass ratio increases, the mode veering region becomes smaller. At $\mu = 3350$, the mode veering region vanishes and the lower boundary of the lock-in region equals the buffet frequency.

7. Conclusions

In this paper, we study the dynamics of a spring suspended NACA0012 airfoil in transonic buffeting flow, especially the physical mechanism underlying the frequency

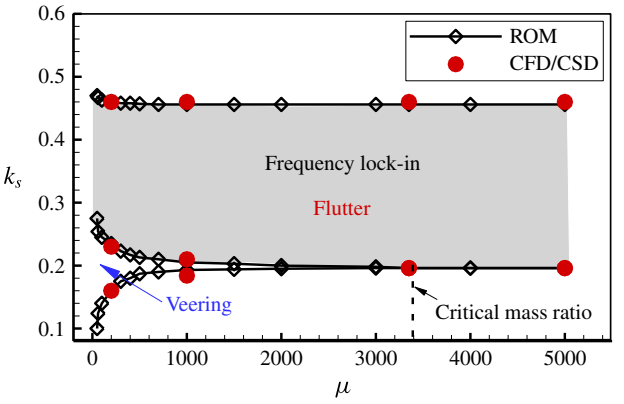

FIGURE 29. (Colour online) Mode veering and frequency lock-in boundaries as functions of the mass ratio.

lock-in phenomenon, by a linear dynamic model. On the basis of the ROM-based aeroelastic model, effects of both the natural frequency of the elastic airfoil and the mass ratio on the dynamics of the airfoil system are investigated by the complex eigenvalue analysis. The coupled CFD/CSD simulation is also performed as a supplement to nonlinear time-domain responses. Main conclusions can be summarized as follows:

(i) The frequency lock-in in transonic buffeting flow is not caused by the resonance, but the linear coupled-mode flutter. In this study, when the frequency ratio is within the range of $1.07 < k_s/k_b < 2.34$, the instability of the structural mode, resulting from the coupling between the fluid and structural modes, is the root cause of the frequency lock-in. This mechanism provides a reasonable explanation why the lock-in region significantly deviates from the resonance point ($k_s/k_b \sim 1$).

(ii) The flutter is in essence the SDOF flutter in an unstable separated flow, different from the classical one (e.g. transonic buzz) which occurs in stable flows. In the present case, there is a competition between two unstable modes – the unstable fluid mode and the unstable structural mode. Therefore, the response of the airfoil system undergoes a conversion from the forced vibration to the self-sustained flutter.

(iii) The frequency lock-in in transonic buffeting flow mainly depends on the linear dynamics instead of the nonlinear characteristics. The linear ROM-based aeroelastic model is proved to be effective as in that it successfully predicts many characteristics in the region of frequency lock-in, including the coupling frequency, the logarithmic increment and the upper flutter boundary, which are mostly consistent with those calculated by the coupled CFD/CSD simulation.

Acknowledgements

This paper is mainly supported by the National Science Fund for Excellent Young Scholars (no. 11622220), 111 project of China (B17037) and National Natural Science Foundation of China (11572252). The first author would also like to acknowledge the sponsorship of the Innovation Foundation for Doctoral Dissertation of Northwestern Polytechnical University (CX201601).

Appendix A. Nomenclature

CFD	computational fluid dynamics
CSD	computational structural dynamics
SDOF	single-degree-of-freedom
ROM	reduced-order model
LCO	limit-cycle oscillation
PSD	power spectrum density
M	Mach number
α	angle of attack
Re	Reynolds number
U_∞	free-stream velocity
ρ	density of the air
T_∞	free-stream temperature
a_∞	free-stream sound speed
c	chord length
b	half chord length, $b = c/2$
f_b	dimensional buffet frequency (Hz)
C_m	pitching moment coefficient
C_l	lift coefficient
na	orders of the ROM
nb	orders of the ROM
θ	pitching angle
μ	mass ratio
η	logarithmic increment
k_s	natural frequency of the elastic airfoil
k_b	buffet frequency
k_{ae}	coupling frequency
k_s^l	lower boundary of the veering region
k_s^m	upper boundary of the veering region
k_s^u	upper flutter boundary

Appendix B. Convergence of the grid and the time step

In order to assess convergence in numerical results, the transonic buffet flow at $M = 0.7$, $\alpha = 5^\circ$ and $Re = 3 \times 10^6$ has been computed for four grids G1 to G4 differed by their spatial resolution. All results presented in the present study are from G3 grid, which is shown in figure 30. Results are detailed in table 1 for nodes of grids and the amplitude of aerodynamic forces, which show that nearly all constants are converged down to the third digit. Results of G3 and G4 grids are almost equal, but the time cost of G3 grid is cheaper. Therefore, the G3 grid is adopted in this research considering the balance between efficiency and accuracy.

Generally, the time step of fluid dynamics is smaller than that of structural dynamics. Therefore, the time step of the present study is decided by the simulation of the buffet flow. For the time convergence of the buffet flow, simulations were run using non-dimensional computational time steps dt ranging from 0.02 to 1, where

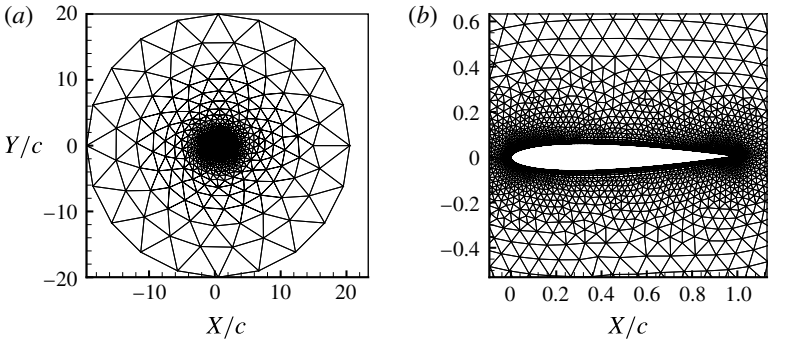

FIGURE 30. (*a*) Overview of the computational grid and (*b*) close-up view of the airfoil.

	G1	G2	G3	G4
Airfoil nodes	90	180	400	600
Surface nodes	4426	9624	25 361	43 004
Amplitude of C_l	0.080	0.100	0.110	0.110
Amplitude of C_m	0.016	0.024	0.024	0.024
Reduced frequency	0.183	0.181	0.180	0.180

TABLE 1. Dependence of the results on different grids differing by their spatial resolution.

Non-dimensional dt	1.0	0.7	0.5	0.1	0.02
Physical dt (s)	2.94×10^{-3}	2.06×10^{-3}	1.47×10^{-3}	2.94×10^{-4}	5.89×10^{-5}
Time averaged C_l	—	0.540	0.574	0.576	0.577
Amplitude of C_l	—	0.09	0.108	0.110	0.110
Time averaged C_m	—	0.146	0.154	0.156	0.156
Amplitude of C_m	—	0.012	0.024	0.024	0.024
Reduced frequency	—	0.16	0.178	0.180	0.180

TABLE 2. Comparison of results at different time steps.

the physical time step is defined as $\mathrm{d}t = \mathrm{d}t_{physics} a_\infty / c$. Table 2 shows the aerodynamic forces, along with the reduced frequency using G3 grid. When the time step increases to 1.0 or a larger one, the CFD solver cannot calculate a buffet. The results converge with a decreasing time step, and a non-dimensional time step no larger than 0.1 (physical time step of 0.00029 s) is adequate for the present simulations.

Appendix C. Validation of aeroelastic models

We choose the BACT case (Rivera *et al.* 1992) to validate the aeroelastic models. Although this case is a two DOF system, procedures for the modelling are the same. That is, it is an alternative validation owing to lack of standard cases for the SDOF system. Relevant parameters of the BACT case are $\mu = 3366$, $r_\alpha^2 = 1.036$ and $\omega_h/\omega_\alpha = 0.6539$ (ω_h and ω_α are natural frequencies of the plunge and pitch mode, respectively) based on the NACA0012 airfoil. Details of other parameters can be found in studies by Rivera *et al.* (1992) and Zhang *et al.* (2015*b*). At $M = 0.71$

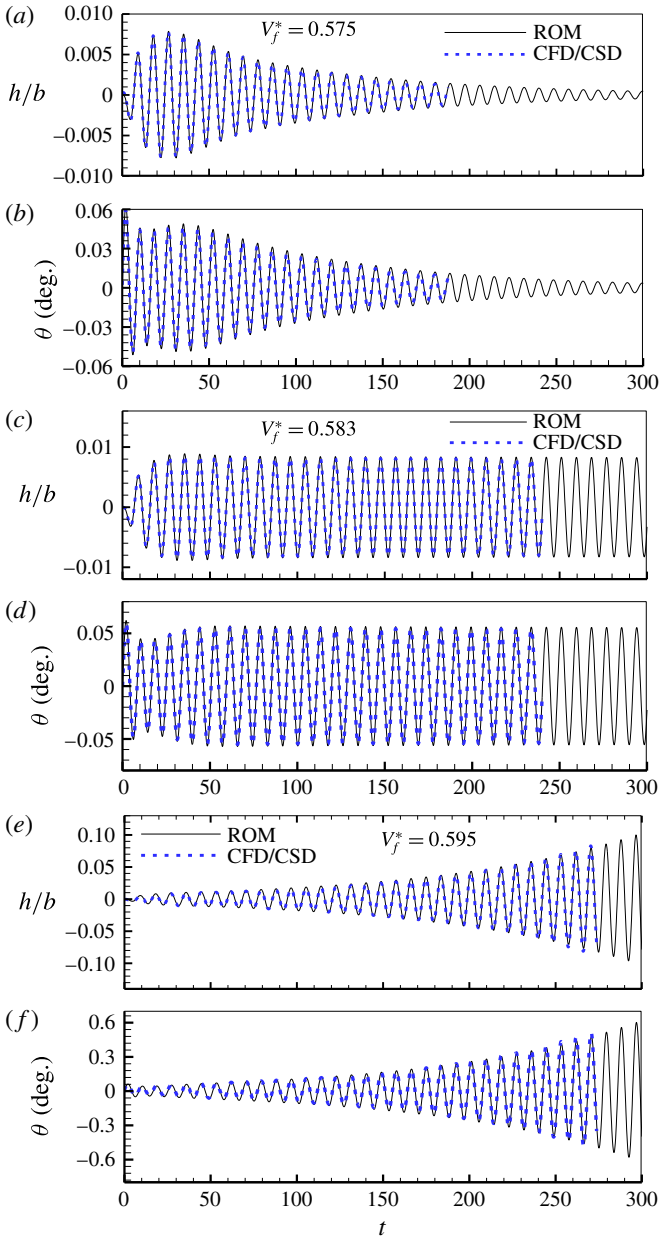

FIGURE 31. (Colour online) Comparison of the time history of the displacement responses between the CFD/CSD simulation and the ROM-based simulation at $M = 0.71$, $\mu = 3363$: (*a*) $V_f^* = 0.575$; (*b*) $V_f^* = 0.583$; and (*c*) $V_f^* = 0.595$.

and $\alpha = 0°$, the calculated reduced flutter velocity based on the coupled CFD/CSD simulation method is 0.585, and the ROM-based one is 0.583, as shown in table 3. Figure 31 shows the comparison of the time history of displacement responses at three velocities between the coupled CFD/CSD simulation and the ROM-based simulation. The ROM-based results can match well with those of the simulation.

	V_f^*	ω_f/ω_α
Experiment	0.594	0.817
CFD/CSD	0.585	0.730
ROM	0.583	0.726

TABLE 3. Comparison of flutter boundaries among the experiment, coupled CFD/CSD simulation and ROM-based aeroelastic model.

REFERENCES

BARAKOS, G. & DRIKAKIS, D. 2000 Numerical simulation of transonic buffet flows using various turbulence closures. *Intl J. Heat Fluid Flow* **21** (5), 620–626.

BARBAGALLO, A., SIPP, D. & SCHMID, P. J. 2009 Closed-loop control of an open cavity flow using reduced-order models. *J. Fluid Mech.* **641**, 1–50.

BARKLEY, D. 2006 Linear analysis of the cylinder wake mean flow. *Europhys. Lett.* **75**, 750–756.

BESEM, F. M., THOMAS, J. P., KIELB, R. E. & DOWELL, E. H. 2016 An aeroelastic model for vortex-induced vibrating cylinders subject to frequency lock-in. *J. Fluids Struct.* **61** (1), 42–59.

BLEVINS, R. D. 1990 *Flow-Induced Vibration*. Van Nostrand Reinhold.

CHEN, L. W., XU, C. Y. & LU, X. Y. 2010 Numerical investigation of the compressible flow past an aerofoil. *J. Fluid Mech.* **643**, 97–126.

CHEN, X. Z. & KAREEM, A. 2003 Curve veering of eigenvalue loci of bridges with aeroelastic effects. *J. Engng Mech. ASCE* **129** (2), 146–159.

CROUCH, J. D., GARBARUK, A. & MAGIDOV, D. 2007 Predicting the onset of flow unsteadiness based on global instability. *J. Comput. Phys.* **224** (2), 924–940.

CROUCH, J. D., GARBARUK, A., MAGIDOV, D. & TRAVIN, A. 2009 Origin of transonic buffet on aerofoils. *J. Fluid Mech.* **628**, 357–369.

DE BOER, A., VAN DER SCHOOT, M. S. & BIJL, H. 2007 Mesh deformation based on radial basis function interpolation. *Comput. Struct.* **85** (11), 784–795.

DECK, S. 2005 Numerical simulation of transonic buffet over a supercritical airfoil. *AIAA J.* **43** (7), 1556–1566.

DE LANGRE, E. 2006 Frequency lock-in is caused by coupled-mode flutter. *J. Fluids Struct.* **22** (6), 783–791.

DOERFFER, P., HIRSCH, C. & DUSSAUGE, J. P. 2010 NACA0012 with aileron unsteady effects of shock wave induced separation. In *Unsteady Effects of Shock Wave Induced Separation*. Springer.

DOWELL, E. H. & HALL, K. C. 2001 Modeling of fluid–structure interaction. *Annu. Rev. Fluid Mech.* **33**, 445–490.

GAO, C. Q., ZHANG, W. W., LIU, Y. L., YE, Z. Y. & JIANG, Y. W. 2015 Numerical study on the correlation of transonic single-degree-of-freedom flutter and buffet. *Sci. China-Phys. Mech. Astron.* **58**, 084701.

GAO, C. Q., ZHANG, W. W. & YE, Z. Y. 2016*a* Numerical study on closed-loop control of transonic buffet suppression by trailing edge flap. *Comput. Fluids* **132**, 32–45.

GAO, C. Q., ZHANG, W. W. & YE, Z. Y. 2016*b* A new viewpoint on the mechanism of transonic single-degree-of-freedom flutter. *Aerosp. Sci. Technol.* **52**, 144–156.

GHOREYSHI, M., JIRASEK, A. & CUMMINGS, R. M. 2014 Reduced order unsteady aerodynamic modeling for stability and control analysis using computational fluid dynamics. *Prog. Aerosp. Sci.* **71**, 167–217.

GONCALVES, E. & HOUDEVILLE, R. 2004 Turbulence model and numerical scheme assessment for buffet computations. *Intl J. Numer. Meth. Fluids* **46** (11), 1127–1152.

GOVARDHAN, R. N. & WILLIAMSON, C. H. K. 2002 Resonance forever: existence of a critical mass and an infinite regime of resonance in vortex-induced vibration. *J. Fluid Mech.* **473**, 147–166.

GOVARDHAN, R. N. & WILLIAMSON, C. H. K. 2006 Defining the 'modified Griffin plot' in vortex-induced vibration: revealing the effect of Reynolds number using controlled damping. *J. Fluid Mech.* **561**, 147–180.

GROSSI, F., BRAZA, M. & HOARAU, Y. 2014 Prediction of transonic buffet by delayed detached-eddy simulation. *AIAA J.* **52** (10), 2300–2312.

HALL, K. C., THOMAS, J. P. & DOWELL, E. H. 2000 Proper orthogonal decomposition technique for transonic unsteady aerodynamic flows. *AIAA J.* **38** (10), 1853–1862.

HARTMANN, A., FELDHUSEN, A. & SCHRÖDER, W. 2013*a* On the interaction of shock waves and sound waves in transonic buffet flow. *Phys. Fluids* **25** (2), 026101.

HARTMANN, A., KLAAS, M. & SCHRÖDER, W. 2013*b* Coupled airfoil heave/pitch oscillations at buffet flow. *AIAA J.* **51** (7), 1542–1552.

HE, S., YANG, Z. C. & GU, Y. S. 2014 Transonic limit cycle oscillation analysis using aerodynamic describe functions and superposition principle. *AIAA J.* **52** (7), 1393–1403.

HUANG, R., LI, H. K., HU, H. Y. & ZHAO, Y. H. 2015 Open/closed-loop aeroservoelastic predictions via nonlinear, reduced-order aerodynamic models. *AIAA J.* **53** (7), 1812–1824.

HYUNG, T. A. & YANNIS, K. 2006 Strong coupled flow/structure interaction with a geometrically conservative ALE scheme on general hybrid meshes. *J. Comput. Phys.* **219** (2), 671–696.

ILLINGWORTH, S. J., MORGANS, A. S. & ROWLEY, C. W. 2012 Feedback control of cavity flow oscillations using simple linear models. *J. Fluid Mech.* **709**, 223–248.

IOVNOVICH, M. & RAVEH, D. E. 2015 Numerical study of shock buffet on three-dimensional wings. *AIAA J.* **53** (2), 449–463.

JACQUIN, L., MOLTON, P., DECK, S., MAURY, B. & SOULEVANT, D. 2009 Experimental study of shock oscillation over a transonic supercritical profile. *AIAA J.* **47** (9), 1985–1994.

JAMESON, A. 1991 Time dependent calculations using multigrid with applications to unsteady flows past airfoils and wings. *AIAA Paper* 91-1259.

JUILLET, F., SCHMID, P. J. & HUERRE, P. 2013 Control of amplifier flows using subspace identification techniques. *J. Fluid Mech.* **725**, 522–565.

KOU, J. Q. & ZHANG, W. W. 2017 An improved criterion to select dominant modes from dynamic mode decomposition. *Eur. J. Mech. (*B*/Fluids)* **62**, 109–129.

LANDON, R. H. 1982 NACA0012 oscillatory and transient pitching. *AGARD Report* 702, AGARD, Dataset 3.

LEE, B. H. K. 2001 Self-sustained shock oscillations on airfoils at transonic speeds. *Prog. Aerosp. Sci.* **37** (2), 147–196.

LI, X. T., LIU, Y. L., KOU, J. Q. & ZHANG, W. W. 2017 Reduced-order thrust modeling for an efficiently flapping airfoil using system identification method. *J. Fluids Struct.* **69**, 137–153.

LIU, Y. L., ZHANG, W. W., JIANG, Y. W. & YE, Z. Y. 2016 A high-order finite volume method on unstructured grids using RBF reconstruction. *Comput. Math. Appl.* **72**, 1096–1117.

LUCIA, D. J., BERAN, P. S. & SILVA, W. A. 2004 Reduced-order modeling: new approachs for computational physics. *Prog. Aerosp. Sci.* **40** (1), 51–117.

MANNARINO, A. & MANTEGAZZA, P. 2014 Nonlinear aeroelastic reduced order modeling by recurrent neural networks. *J. Fluids Struct.* **48**, 103–121.

MCDEVITT, J. B. & OKUNO, A. F. 1985 Static and dynamic pressure measurements on a NACA 0012 airfoil in the Ames high Reynolds number facility. *Tech. Paper* 2485. NASA.

MELIGA, P. & CHOMAZ, J. 2011 An asymptotic expansion for the vortex-induced vibrations of a circular cylinder. *J. Fluid Mech.* **671**, 137–167.

NGUYEN, T., KOIDE, M., YAMADA, S., TAKAHASHI, T. & SHIRAKASHI, M. 2012 Influence of mass and damping ratios on VIVs of a cylinder with a downstream counterpart in cruciform arrangement. *J. Fluids Struct.* **28** (1), 40–55.

PERKINS, N. C. & MOTE, C. D. JR. 1986 Comments on curve veering in eigenvalues problems. *J. Sound Vib.* **106** (3), 451–463.

PRASANTH, T. K., PREMCHANDRAN, V. & MITTAL, S. 2011 Hysteresis in vortex-induced vibrations: critical blockage and effect of m^*. *J. Fluid Mech.* **671**, 207–225.

QUAN, J. G., ZHANG, W. W., GAO, C. Q. & YE, Z. Y. 2016 Characteristic analysis of lock-in for an elastically suspended airfoil in transonic buffet flow. *Chin. J. Aeronaut.* **29** (1), 129–143.

RAVEH, D. E. & DOWELL, E. H. 2011 Frequency lock-in phenomenon for oscillating airfoils in buffeting flows. *J. Fluids Struct.* **27** (1), 89–104.

RAVEH, D. E. & DOWELL, E. H. 2014 Aeroelastic responses of elastically suspended airfoil systems in transonic buffeting flows. *AIAA J.* **52** (5), 926–934.

RIVERA, J. A., DANSBERRY, B. E., BENNETT, R. M., DURHAM, M. H. & SILVA, W. A. 1992 NACA 0012 benchmark model experimental flutter results with unsteady pressure distributions. *AIAA Paper* AIAA-92-2396-CP.

SARTOR, F., METTOT, C. & SIPP, D. 2015*a* Stability, receptivity, and sensitivity analyses of buffeting transonic flow over a profile. *AIAA J.* **53** (7), 1980–1993.

SARTOR, F., METTOT, C., BUR, R. & SIPP, D. 2015*b* Unsteadiness in transonic shock-wave/boundary-layer interactions: experimental investigation and global stability analysis. *J. Fluid Mech.* **781**, 550–577.

SARTOR, F. & TIMME, S. 2017 Delayed detached–eddy simulation of shock buffet on half wing–body configuration. *AIAA J.* doi:10.2514/1.J055186.

SENGUPTA, T. K., BHOLE, A. & SREEJITH, N. A. 2013 Direct numerical simulation of 2D transonic flows around airfoils. *Comput. Fluids* **88**, 19–37.

SINGH, S. P. & MITTAL, S. 2005 Vortex-induced oscillations at low Reynolds numbers: hysteresis and vortex-shedding modes. *J. Fluids Struct.* **20** (8), 1085–1104.

SIPP, D., MARQUET, O., MELIGA, P. & BARBAGALLO, A. 2010 Dynamics and control of global instabilities in open-flows: a linearized approach. *Appl. Mech. Rev.* **63**, 030801.

SIPP, D. 2012 Open-loop control of cavity oscillations with harmonic forcings. *J. Fluid Mech.* **708**, 439–468.

SODA, A. & VOSS, R. 2005 Analysis of transonic aerodynamic interference in the wing-nacelle region for a generic transport aircraft. In *IFASD, Munich, Germany*.

SPALART, P. & ALLMARAS, S. 1992 A one-equation turbulence model for aerodynamic flows. *AIAA Paper* 92-0439.

THOMAS, J. P., DOWELL, E. H. & HALL, K. C. 2006 Static/dynamic correction approach for reduced-order modeling of unsteady aerodynamics. *J. Aircraft* **43** (4), 865–878.

VIJAYANN, K. & WOODHOUSE, J. 2014 Shock amplification, curve veering and the role of damping. *J. Sound Vib.* **333** (5), 1379–1389.

WANG, G., MIAN, H. H. & YE, Z. Y. 2015 Improved point selection method for hybrid-unstructured mesh deformation using radial basis functions. *AIAA J.* **53** (4), 1016–1025.

WILLDEN, R. H. J. & GRAHAM, J. M. R. 2006 Three distinct response regimes for the transverse vortex-induced vibrations of circular cylinders at low Reynolds numbers. *J. Fluids Struct.* **22** (6), 885–895.

XIAO, Q., TSAI, H. M. & LIU, F. 2006 Numerical study of transonic buffet on a supercritical airfoil. *AIAA J.* **44** (3), 620–628.

ZHANG, W. W., CHEN, K. J. & YE, Z. Y. 2015*a* Unsteady aerodynamic reduced-order modeling of an aeroelastic wing using arbitrary mode shapes. *J. Fluids Struct.* **58**, 254–270.

ZHANG, W. W., GAO, C. Q., LIU, Y. L., YE, Z. Y. & JIANG, Y. W. 2015*b* The interaction between transonic buffet and flutter. *Nonlinear Dyn.* **82** (4), 1851–1865.

ZHANG, W. W., JIANG, Y. W. & YE, Z. Y. 2007 Two better loosely coupled solution algorithms of CFD based aeroelastic simulation. *Engng Appl. Comput. Fluid.* **1** (4), 253–262.

ZHANG, W. W., LI, X. T., YE, Z. Y. & JIANG, Y. W. 2015*c* Mechanism of frequency lock-in in vortex-induced vibrations at low Reynolds numbers. *J. Fluid Mech.* **783**, 77–102.

ZHANG, W. W., WANG, B. B. & YE, Z. Y. 2012 Highly efficient numerical method for limit cycle flutter analysis based on nonlinear aerodynamic reduced-order models. *AIAA J.* **50** (5), 1019–1028.

ZHANG, W. W. & YE, Z. Y. 2007 Control law design for transonic aeroservoelasticity. *Aerosp. Sci. Technol.* **11** (2), 136–145.

ZHANG, W. W., YE, Z. Y. & ZHANG, C. A. 2009 Aeroservoelastic analysis for transonic missile based on computational fluid dynamics. *J. Aircraft.* **46** (6), 2178–2183.